AALTO UNIVERSITY SCHOOL OF SCIENCE AND TECHNOLOGY
Faculty of electronics, telecommunications and automation

Eero Huotilainen

COMPUTED TOMOGRAPHY BASED TALOCRURAL JOINT MOTION CAPTURE FOR PATIENT-SPECIFIC EXTERNAL FIXATOR DESIGN

Master’s Thesis

Espoo, August 19th, 2011

Supervisor: Professor Ari Koskelainen
Instructor: Jukka Tuomi

Aalto-yliopisto

AALTO UNIVERSITY ABSTRACT

Author:	Eero Huotilainen
Title:	Computed tomography based talocrural joint motion capture for patient-specific external fixator design
Date:	19.8.2011 Language: English Pages: 8+50+2
Instructor:	Lic.Tech. Jukka Tuomi
Supervisor:	Prof. Ari Koskelainen

Pilon fracture is a severe ankle trauma, which demands instant orthopedic treatment. After the trauma, the ankle needs to be shielded from load, but to maximize the flows of blood and nutrients, ankle should also be allowed to move in a controlled fashion, e.g. around one axis. External, rotating fixators exist for this purpose. Utilizing additive manufacturing techniques, a patient-specific fixator can be designed. It aims to mimic the natural range of motion, and thus minimize the motion resistance. Prior to the fixator fabrication, the location and orientation of the talocrural joint axis in different phases of the motion needs to be determined.

In this thesis, a computed tomography based measurement method was developed and piloted. Two subjects were scanned with a cone-beam CT device: the first subject in three stances (full dorsiflexion, neutral, full plantarflexion), and the second one in five stances (aforementioned three, and in addition, half plantarflexion and half dorsiflexion).

After this, the tibia and talus bones were segmented. The corresponding bones in two consecutive poses (full dorsiflexion-half dorsiflexion, half dorsiflexion-neutral, etc.) were registered in respect to each other. These registrations produced two transform matrices, which were used to calculate the finite helical axis (location and orientation) of each phase of the motion.

The technique yielded sensible results, thus further development is recommended. The actual accuracy remains unknown, and needs to be determined e.g. by larger patient pool. This is complicated by the radiation burden involved with CT imaging.

Key words: talocrural joint, ankle fracture, rapid prototyping, additive manufacturing, computed tomography (CT)

AALTO-YLIOPISTO TIIVISTELMÄ

Tekijä: Eero Huotilainen
Nimi: Nilkkanivelen tietokonetomografia-liikemallinnus
potilaskohtaisen ulkoisen tuen suunnittelua varten
Pvm: 19.8.2011 Kieli: englanti Sivut: 8+50+2

Ohjaaja: Tekn.lis. Jukka Tuomi
Valvoja: Prof. Ari Koskelainen

Pilon-murtumat ovat vaikeita, välitöntä ortopedista hoitoa vaativia nilkan traumoja. Trauman jälkeen nilkka on tuettava, mutta ravintoaineiden ja veren virtauksen parantamiseksi nilkan olisi suotavaa saada liikkua kontrolloidusti, esimerkiksi yhden akselin ympäri. Tätä varten on kehitetty kääntyviä, ulkoisia nilkkatukia. Ainetta lisäävän valmistuksen keinoin on mahdollista luoda jokaiselle potilaalle yksilöllinen tuki, joka seuraa potilaan nilkan luonnollista liikerataa.Tätä varten on selvitettävä potilaan ylemmän nilkkanivelen kääntöakselin paikka sekä suunta eri vaiheissa nilkan koukistusta ja ojennusta.

Tässä diplomityössä suunniteltiin ja toteutettiin tietokonetomografiaan perustuva mittausmenetelmä. Koehenkilöitä oli kaksi: ensimmäisen nilkka kuvattiin kartiokeila-TT-laitteella kolmessa asennossa (äärikoukistus, neutraali, ääriojennus), ja toisen viidessä (edellämainitut asennot, sekä puolittainen koukistus ja puolittainen ojennus).

Tämän jälkeen kuvista segmentoitiin sääriluu sekä telaluu. Kahden peräkkäisen asennon (ääriojennus-puolittainen ojennus, puolittainen ojennus-neutraali, jne.) luut kohdennettiin toistensa suhteen. Nämä kohdennukset tuottivat kaksi muunnosmatriisia, joiden avulla laskettiin liikkeen kunkin vaiheen kääntöakselin (finite helical axis, FHA) paikka sekä suunta.

Menetelmä tuotti järkeviä tuloksia, joten lisäkehitystä suositellaan. Tekniikan oikea tarkkuus on selvitettävä esimerkiksi toistokokein, mutta näitä rajoittaa tietokonetomografiakuvaukseen liittyvä säderasitus.

Avainsanat: *nilkkanivel, murtuma, pikavalmistus, ainetta lisäävä valmistus, tietokonetomografia (TT)*

Acknowledgements

I would like to thank warmly my supervising professor Ari Koskelainen, and my instructor Jukka Tuomi, as well as everyone else in the Integrated Design and Manufacturing research group.

In addition, my gratitude goes out to Jan Lindahl, Jari Salo, and Seppo Koskinen of Hospital District of Helsinki and Uusimaa, Mika Pollari for his advices concerning medical image registration problems, and my friends and family for their support during this project.

in Espoo, 19.8.2011

Eero Huotilainen

Contents

Abstract......ii

Tiivistelmä......iii

Acknowledgements......iv

Contents......v

Glossary and abbreviations......vii

1 Introduction......1

2 The ankle joint complex and talocrural joint motion

2.1 The ankle joint complex......4

2.2 Literature on the talocrural joint motion......5

3 Patient-specificity by additive manufacturing

3.1 Additive manufacturing and how it can benefit orthopedic treatment......7

3.2 Phases of additive manufacturing......8

3.3 Medical applications of additive manufacturing......8

3.4 Additive manufacturing technologies......9

3.5 Requirements for additive manufacturing design input......10

4 Reverse engineering of joint motion: rigid body kinematics and motion capture techniques

4.1 Rigid body kinematics in joint motion analysis......12

4.2 Motion capture techniques......12

4.3 Direct vs. indirect motion capture......15

4.4 Contralateral joint comparison......15

5 Dynamic and quasi-dynamic medical imaging

5.1 Dynamic medical imaging modalities......17

5.2 X-ray and computed tomography......18

5.3 Cone-beam computed tomography (CBCT)......20

5.4 Image segmentation......21

5.5 Image registration......21

6 Materials and methods

6.1 Case study description......23

6.2 Methodology......26

6.3 Transformation matrix algebra 29

7 Results

7.1 Segmentation results.. 32
7.2 Registration results... 35
7.3 Joint axis calculations, subject 1 35
7.4 Joint axis calculations, subject 2 38
7.5 Accuracy and reliability of the method 40
7.6 Error analysis... 43
7.7 The applicability of the method for other joints 44
8 Conclusions 45
References 46

Appendices

Appendix A: IRTK input parameters.. 51
Appendix B: Transformation matrices of subject 2 52

Glossary and abbreviations

AM	additive manufacturing
anterior	in the front; in this thesis towards the toes of the patient
CAD / CAM	Computer-Aided Design / Computer-Aided Manufacturing
CaFi	calcaneofibular ligament
calcaneus	heel bone
contralateral	on the other (opposite) side; in this thesis referring to the intact ankle joint complex
CT	computed tomography
degrees of freedom (DoF)	the number of independent displacements and/or rotations that determine completely the spatial state (position and orientation) of an object
distal	further from something (in this thesis head)
dorsiflexion	tilting of the foot backwards
femur	thigh bone
FHA	finite helical axis
fibula	calf bone
IHA	instantaneous helical axis
inferior	below; in this thesis towards the soles of the patient
ipsilateral	on the same side; in this thesis referring to the injured ankle joint complex
MRI	magnetic resonance imaging

patella	knee cap
plantarflexion	tilting of the foot forwards
posterior	in the back; in this thesis towards the heel of the patient
proximal	closer to something (in this thesis head)
RM	rapid manufacturing
ROI	region of interest
RP	rapid prototyping
STL	*de facto* RP industry standard format for 3D model data; represents surfaces as collections of triangles with three points (vertices) and a normal unit vector outwards from the object
subtalar joint	a.k.a. talocalcaneal joint: a joint between the talus and the calcaneus
superior	above; in this thesis towards the head of the patient
talocrural joint	ankle joint: synovial hinge joint connecting the distal ends of the tibia and fibula in the lower limb with the proximal end of the talus bone in the foot
tibia	shinbone
tibial mortise	inferior/distal surface of the tibia, the top of the talocrural articular volume
TiCa	tibiocalcaneal ligament
trochlea tali	superior/proximal surface of the talus, the bottom of the talocrural articular volume
VOI	voxel/volume of interest

1 Introduction

The pilon fracture is a severe rupture of the distal articular surface of the tibia (shinbone). It is typically caused by a sudden vertical impact which drives the tibia into the talus bone, causing the shattering of the distal tibia and breakage of articular cartilage. Types of shattering can be divided into three classes: extra-articular, partial articular fracture, and complete articular fracture [Chowdhry and Porter, 2010], [Müller and Nerlich, 2010], depending on the level of articular surface fragmentation. The more there is articular surface displacement, the more likely is a possibility of severe cartilage damage. Figure 1 illustrates the possible fragmentation levels according to the AO classification.

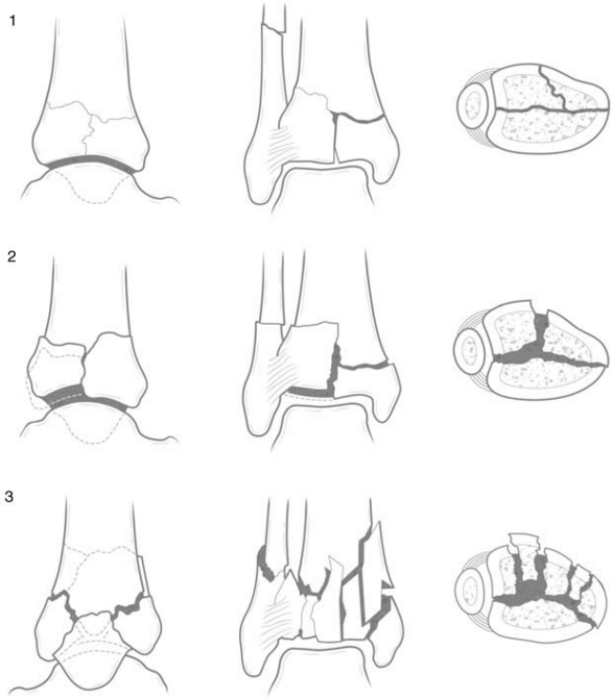

Figure 1: Pilon fracture types by AO classification. Top: extra-articular fracture with little or no articular displacement. Middle: partial articular fracture with moderate articular displacement. Bottom: complete fragmentation of the distal tibia. [Chowdhry and Porter, 2010], [Rüedi and Allgöwer, 1969]

The healing of broken cartilage is a slow process which may take several months. In case the cartilage does not recover, a disablement called arthrosis may follow in few years. During the cartilage healing period, the fracture needs to be shielded from excessive loading, which can be achieved by e.g. plaster cast. However, for optimal healing to take place, a steady flow of oxygen and nutrition to the articular cartilage should be ensured [O'Hara et al., 1990], [Salter et al., 1980]. This can be achieved with a fixator which allows a certain restricted motion, e.g. around one axis – it can be thought as a cyclic pump which drives the nutrition into the tissue and blood out [Bottlang et al., 1999]. Most hinge fixators are factory-made, one-size-fits-all solutions which are placed in merely an approximate orientation and location. This creates a lot of unwanted motion resistance, and thus does not allow for patient’s ankle to move in its natural way, but it has been considered accurate enough since the clinicians do not use very precise methods for the axis definition anyway – it is mostly estimated visually. This method may locate the measured axis up to several centimeters from the real joint axis.

Although corrections have been proposed to the estimation process [Bruening et al., 2008], Fitzpatrick and colleagues [Fitzpatrick et al., 1995a], [Fitzpatrick et al., 1995b] state that patient-specific hinge position is superior to traditional horizontal axis in external fixator design. Bottlang agrees: it is crucial to find an anatomically correct axis of revolution. Malpositioning a hinge by merely 1 cm causes five times more motion resistance compared to the optimal fixator hinge position [Bottlang et al., 1999] – a significant amount, which most likely slows down the healing process of the patient. The primary research question of this thesis is: “Can the movement of an arbitrary joint be tracked accurately and non-invasively in order to define the location and orientation of the joint axes?” As a case study, the motion of the ankle joint, also known as the talocrural joint, is defined. Ankle joint complex can be considered challenging. The range of motion in talocrural joint is usually relatively small, typically around twenty degrees. Therefore, even minuscule errors in the motion analysis may accumulate.

Adding degrees of freedom to the system leads usually to more complicated fixator designs. The relationship between the two is more of an exponential than linear nature – a fully mobile (i.e. 6 DoF) axis system is extremely complex, and in practice extremely expensive. Hence, a tradeoff needs to be made between as-accurate-as-possible anatomical joint motion imitation and feasible mechanical design. This thesis concludes with some estimates about this tradeoff; that is, which of the six available degrees of freedom should be left fixed and which of them should be mobile.

The following list describes a proposed process for CT-based joint motion capture that could be performed preliminary for various risk groups, such as athletes. After a possible injury, a rapid creation of patient-specific support would be straightforward, and the custom-made fixator would mimic accurately the pre-accident joint motion of the patient.

1. Preliminary CT scan (multiple images at different points in the arc of motion, 3 being the minimum amount in order to capture both the location and the orientation of the helical axis)
2. Bone segmentation and definition of frames of reference (FORs)
3. Segment/FOR registration
4. Computing the joint kinematics by relative movements of segments/FORs

time **Accident leading to a fracture**

5. Insertion of the bone nails
6. CT scan (1 image)
7. Joint kinematics data + bone nail locations => additive manufacturing parameters
8. Additive manufacture of the customizable parts and installation of the support

Alternatively, in order to avoid unnecessary work, one could also perform preliminarily only the first step (first CT scanning) and do the segmentation, registration and kinematics computing *after* the accident, i.e. if needed. However, this course of action is not recommended since it prevents reimaging the patient in case the segmentation, for example, cannot be performed because of blurry or ambiguous images.

The first (pre-accident) steps need to be as non-invasive, safe and convenient as possible for the patient. Thus, e.g. the insertion of bone nails or pins is unacceptable at this stage. However, after the accident more invasive measures might be performed. The imaging modality of choice in this thesis is computed tomography. The reason for this is both its noninvasiveness and its widespread availability in hospital environments. According to Blankevoort [Blankevoort et al, 2008], its accuracy should be adequate.

The following four chapters will provide a brief overview of the relevant literature and prior research in this area. First, the ankle joint complex, and especially the talocrural joint, is described in greater detail. After that, additive manufacturing techniques are introduced, as well as different methods for (joint) motion capture and basics of computed tomography and CBCT (the device used in this thesis' case study).

The case study materials and methods are presented in the chapter 6. The subsequent chapter ("Results") presents the results of the study. Finally, conclusions are made and recommendations for further research are given.

2. The ankle joint complex and talocrural joint motion

2.1 The ankle joint complex

Ankle joint complex is a delicate mechanism comprised of several joints controlled by various muscles and guided by articular surfaces and ligaments, most notably the tibiocalcaneal (TiCa) and calcaneofibular (CaFi) ligaments. Figure 2 depicts an ankle with its main bones – tibia (the shin bone), fibula (the calf bone), talus, and calcaneus (the heel bone) – marked.

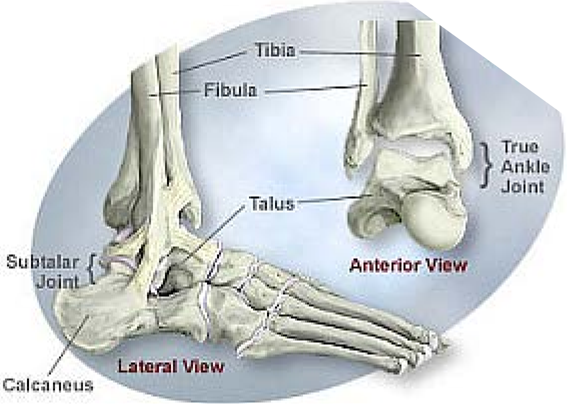

Figure 2: Ankle bones, the talocrural joint (true ankle joint) and the subtalar joint. [Southern California Orthopedic Institute, 2004]

The motion of human ankle is created by two separate joints: The talocrural joint, or true ankle joint, is approximately a hinge joint between talus and the distal ends of tibia and fibula, which enables the up-and-down motion of the foot. Tilting the foot forwards (toes moving down) is called plantarflexion (PF), and tilting it backwards (toes moving up) is called dorsiflexion (DF). [Nienstedt et al., 1999]

The other major ankle joint is the subtalar joint. It connects the talus with the calcaneus, hence it is known also as the talocalcaneal joint. It allows the sideways motion of the foot. These types of motion are called inversion and eversion, or movement of the sole of the foot towards and away the median plane, respectively. The subtalar joint plays a minor part in dorsiflexion and plantarflexion. However, we can assume that the analysis of talocrural motion is sufficient for our study, since the majority of the motion is located there [Mattingly et al., 2006]. The function of the subtalar joint seems to be more of a balancing joint in DF and PF. [Leardini et al., 1999]

The anatomical terms of locations and directions differ somewhat between studies. In this thesis, the following nomenclature is used: The anteroposterior (AP) axis goes from the toes (anterior) to the heel (posterior). The inferior-superior axis runs from the sole of the foot upwards the tibia, and the mediolateral axis of the right leg runs laterally from the left side of the ankle to the right – i.e. medial refers to the side on the inner side of the foot, and the opposite is the lateral side.

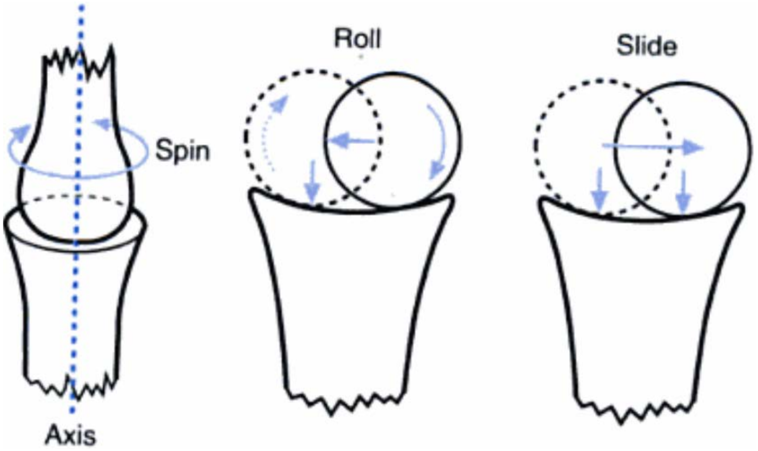

Figure 3: Types of motion at articular surfaces.

Articular surfaces exhibit in general three kinds of relative motion: spinning around the longitudinal axis, rolling, and sliding in the joint socket (see figure 3 for clarification).

In the talocrural joint, the joint socket is formed by the inferior ends of the tibia and fibula – this is also called the tibial mortise. Against it, the pulley-shaped surface of the talus, or trochlea tali, is articulated. The simplest talocrural joint models describe the joint as a uniaxial synovial hinge joint [Oatis, 1988] with only roll motion on sagittal plane (PF, DF). Our group had initially an idea about a symmetrical, barrel-like talus shape, on which the tibial mortise would rotate in a predictable manner and around a fixed axis – this belief was rooted in evolutionary reasoning and knowledge of mechanical engineering. However, as the research progressed, it became apparent that nature is somewhat more complicated.

Trochlea tali, the superior surface of the talus is actually wedge-shaped, anteriorly wider than posteriorly, and slightly concave side to side. The irregular shape makes real articulation much more complex [Corazza et al., 2005]. Spin motion can be neglected, but while the majority of the motion consists of rolling, a significant amount of slide seems to be present especially near the extreme dorsiflexed and plantarflexed stances.

2.2 Literature on the talocrural joint motion

Both inter-study and intra-study variation concerning the talocrural joint motion can be considered large – differing conditions such as joint loading factors (loaded, passive, walking, running, etc.), measurement method (in vivo or in vitro), or subject age have a substantial effect on the results.

The consensus in both traditional and contemporary orthopedic textbooks [Inman, 2002] places the talocrural joint axis passing through the distal ends of the lateral and medial malleoli, although some orthopaedists have questioned this, as well as Lundberg et al. in their milestone research [Lundberg et al., 1989], in which they used tantal beads and in vivo radiostereophotogrammetric (RSA) analysis. Radiostereophotogrammetry utilizes two x-ray tubes and detector plates orthogonal to each other (e.g. on posterior and right-lateral side of the foot), which allows the tracking of the spatial locations of tantal beads in three dimensions. Lundberg et al. found that the talocrural joint axis alters considerably during the arc of motion; it is different for plantarflexion and dorsiflexion, and the exact place and rate of axis change varies between individuals. This supports the idea of designing an external fixator with non-rigid degrees of freedom (mobile axis).

Sheehan [Sheehan, 2010] used successfully a cine-phase contrast (dynamic) magnetic resonance imaging device to acquire instantaneous helical axes (IHA) of the talocrural and subtalar joints. They concluded that the talocrural motion is close to fixed-hinge joint, whereas subtalar joint is not. Other measurement methods have been electromagnetic tracking [Wong et al., 2005], optical camera system [Arndt et al., 2006], and ultrasound emitters [Peolsson et al., 2010]. Most of the studies are qualitative, merely describing the motions and giving little empirical data. This is due to the large variation between subjects.

3 Patient-specificity by additive manufacturing

3.1 Additive manufacturing and how it can benefit orthopedic treatment

Additive manufacturing is such an integral part of the proposed treatment process – highlighting patient-specificity – that the concept of AM will be described (albeit very briefly) in this chapter. Manufacturing technologies in mechanical engineering have traditionally been classified to material forming (additive), material removing (subtractive) and formative technologies (figure 4). Examples of subtractive fabrication processes include milling, drilling, turning, sawing, grinding, and laser cutting. Additive and formative fabrication techniques include methods such as casting and bending, respectively. [TEKES, 1999]

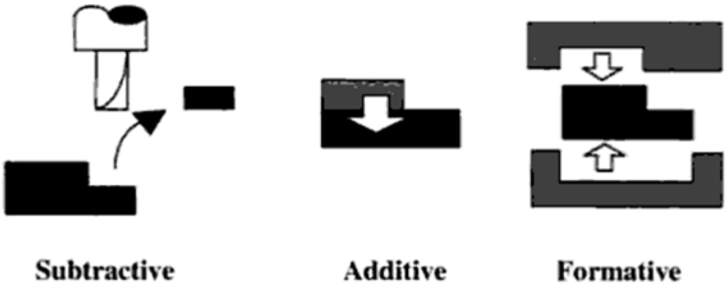

Figure 4: Three types of fundamental fabrication processes.

Rapid Manufacturing (RM) – also known as Rapid Prototyping and Manufacturing, Layer Manufacturing, Free Form Fabrication (FFF) – is a collection of manufacturing technologies describing the automatic layer-by-layer production of physical parts, based on a three-dimensional CAD (computer assisted design) model. While the earlier term, Rapid Prototyping (RP), referred primarily to the fabrication of conceptual design models and prototypes in the early phases of product development processes, the term rapid manufacturing (RM) is more appropriate today since the concept covers a wider range of applications and needs, ranging from customized parts to even consumer goods. [Wohlers, 2010]

Despite its name, rapid manufacturing is not exactly instantaneous. In the actual 3D printing phase, fastest rapid manufacturing systems add around 80 cubic centimeters of metal or 150-200 cubic centimeters of plastic per hour. To put this in perspective, the production time of a typical square-shaped, 25 cm wide and 5 millimeters thick mouse pad could last over two hours. This rough estimation should serve as a down-to-earth reminder of the limitations of the current technologies, and because of this, we prefer to use the term additive manufacturing instead.

Considering the aforementioned lack of speed, additive manufacturing of the whole fixator in pilon fracture treatment would not really make much sense. Instead, a factory made Ilizahrov fixator framework will be used, and solely certain smallish junction parts will be customized by additive manufacturing. Hence, this thesis is essentially about finding the right dimensions for these patient-specific pieces. This hybrid approach combines the best of both manufacturing processes: the low unit cost of standardized parts (achieved by mass production) and the ability to customize the fixator according to the patient-specific range of motion (achieved by additive manufacturing). A widely used term for the use of flexible computer-aided manufacturing systems to achieve custom output is mass customization.

3.2 Phases of additive manufacturing

In general, the additive manufacturing process phases are: 1) gathering of physical data (e.g. by scanning the dimensions of an object with a 3D scanner), 2) the modeling of the object by creating a three-dimensional computer aided design (CAD) model and 3) manufacturing the object ("3D printing"). The following three subchapters cover these phases in reverse chronological order: starting with medical applications of AM, following with the 3D printing (Ch. 3.4 "AM technologies") and the CAD model (Ch. 3.5 "Requirements for AM design input") phases. This backwards order was chosen to emphasize applications over technologies, and also, to the help reader pay attention to the importance of different inputs in the chain, and what is required of them. The rest of this thesis concerns the first step of the process: the medical imaging phase.

3.3 Medical applications of additive manufacturing

Medical applications of rapid prototyping and manufacturing, and additive manufacturing have many promising advantages over traditional manufacturing processes [Giannatsis and Dedoussis, 2009]. The main advantage is the ability to create completely freeform 3D shapes, with in theory as complex structures as the designer wants (practical reasons might prevent this, e.g. the CAD software running out of memory, or the AM device being not able to achieve as fine resolution as needed). This allows creative *ad hoc* solutions for various medical problems and greatly improves the patient care. A range of materials used in additive manufacturing can already be sterilized, and a constant research focus is held to further improve the biodegradability and biocompability of materials to be used in AM.

Tuomi and colleagues have proposed a five-category classification for medical applications of additive manufacturing. [Tuomi et al., 2010]:

1. *Models for preoperative planning, education and training*
   Rapid prototyping enables manufacturing of surgical models for preoperative planning and simulation [Petzold et al., 1999], and educating of students. Such desired qualities as anatomical correspondence to the modeled body/organ, and realistic haptic response of the model are available. Hard tissue mimicking materials (plastics, ceramics, etc.) are widely available, and in the future, spongy soft tissue –like materials will most likely be developed as well.

2. *Inert implants*
   Since the techniques allow the creation of completely arbitrary shapes, fully customized implant design is one of the main uses of AM technologies today in the medical milieu.

3. *Tools, instruments and parts for medical devices*
   Rapid prototyping and additive manufacturing techniques might also be used for creation of tools and hardware for medical purposes. An example of these would be a rapid prototyping of an operation specific custom instrument.

4. *Medical aids, supportive guides, splints and prostheses*
   The case study in this thesis concerns an example of this application class: an external ankle support device. Other types of applications include custom prostheses and splints.

5. *Biomanufacturing*
   This is probably the most challenging – technologically speaking – of the five proposed categories. Biomanufacturing technologies cover the research areas of freeform cell culturing (in additive manufactured 3D scaffolds [Mironov et al., 2009]), and in the long run, even additive manufacturing of artificial human tissue.

3.4 Additive manufacturing technologies

Rapid prototyping and additive manufacturing technologies include a wide array of competing additive layering techniques. Their operating methods vary considerably. [Kruth et al., 1998]

Stereolithography (SLA)
One of the first rapid manufacturing processes, stereolithography, was established in the 1980’s and became somewhat a synonym for 3D printing for a long period. The manufacturing process borrowed also its name to the industry-standard file type for the data transfer between computer assisted design (CAD) system and rapid manufacturing devices – the STL triangular surface representation. The technology utilizes a vat of liquid resin, which is cured (i.e. solidified) layer-by-layer by an UV laser beam.

Selective Laser Sintering (SLS)
Laser sintering and stereolithoraphy are today the main additive manufacturing technologies. SLS is based on a pulsed laser beam which heats powdered plastic, ceramic, or metal laid on a fabrication bed, ultimately melting the powder particles according to desired 3D form.

Electron Beam Melting (EBM)
Electron beam melting technology utilizes – like SLS – powder (solely metal) to manufacture objects. Instead of laser, the powder is melted by an electron beam in a vacuum, resulting in stronger parts than laser sintering can provide.

Fused Deposition Modeling (FDM)
Fused deposition modeling constructs parts by thermoplastics that are heated, liquefied, and extruded through a nozzle. The extrusion head moves in two (x, y) directions according to the inputted CAD model, while the third (z) direction is controlled by raising and lowering fabrication bed.

3.5 Requirements for additive manufacturing design input

In order to fabricate objects by additive manufacturing, a certain input is required – e.g. the original object to be recreated. The RP system requires electronic information describing the dimensions and characteristics of the physical object. The two starting points are either a computer model or a physical model. While the aforementioned option means creating a CAD model (either a surface model or a solid model) by a computer from a scratch, the latter option is a much more complicated process (and also the main research problem in this thesis): By reverse engineering, one must transform a physical object (or body part) to a digitized point cloud, which can then be reconstructed in a CAD system.

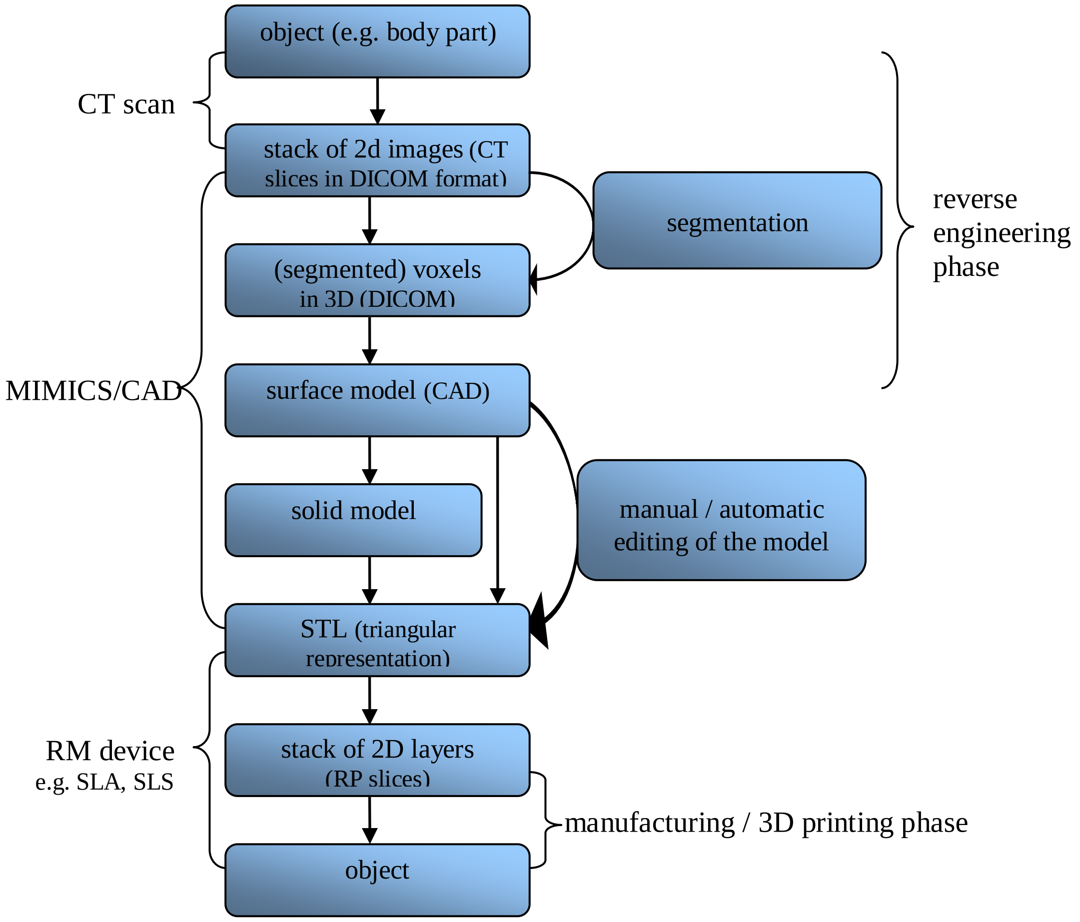

Figure 5: The process flow for additive manufacturing (object recreation).

A vast amount of technologies exist for reverse engineering problems: some examples include CMM (coordinate measuring machine) and a laser digitizer (laser scanner). Lorensen and Cline proposed [Lorensen and Cline, 1987] an algorithm entitled "marching cubes" for the digitalization of medical data. The whole process – see figure 6 – is divided into four phases: data acquisition (e.g. by computed tomography scan), image processing, surface construction (marching cubes algorithm), and finally, displaying the rendered image (or, as in our case, sending the CAD model to the additive manufacturing equipment).

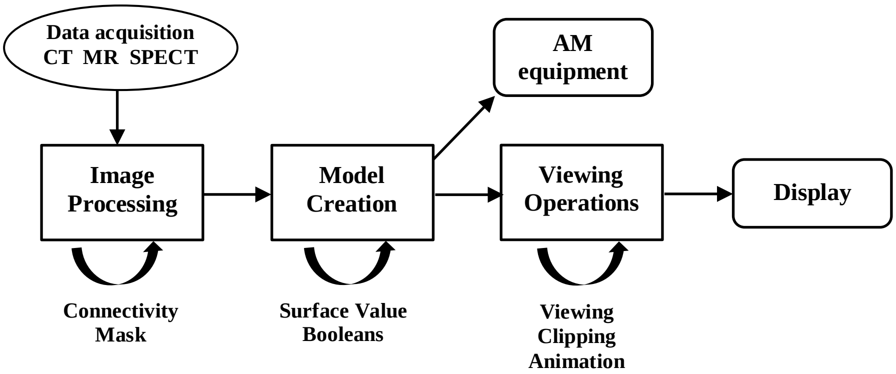

Figure 6: Phases of 3D data acquisition and digitalization.

4 Reverse engineering of joint motion: rigid body kinematics and motion capture techniques

4.1 Rigid body kinematics in joint motion analysis

Any displacement of a rigid body can be effected by a rotation about a unique axis and independently, a translation parallel to that axis [Davidson and Hunt, 2004]. This representation is called either the screw, twist or helical motion. We will use the term helical motion. The values of the helical rotation and translation are independent of the chosen reference frame. The helical axes can be either finite or instantaneous. At any given time, the axis about which the joint movement happens is termed instantaneous helical axis (IHA), while a finite helical axis (FHA) describes a motion step and thus is an approximation of the time integral of the instantaneous helical axes between those endpoints. In this thesis, the finite helical axis method is utilized.

4.2 Motion capture techniques

As earlier was stated, there are multiple methods for solving reverse engineering problems. Motion and trajectories can be imaged e.g. by:

- inertial methods
- mechanical methods
- optical methods
- magnetic methods
- medical imaging
- other techniques

Inertial methods

This class of techniques is based on usage of sensors, such as accelerometers, gyroscopes and magnetometers. Accelerometers are sensors that contain a spring-suspended mass which is allowed to move in one direction. The displacement of the mass and known (or estimated) gravity vector (Earth’s gravitational pull) define the proper acceleration component in the sensitive direction. Combining three accelerometers, one acquires full 3-degrees-of-freedom acceleration measurement. Additionally, there are available 3D accelerometers which measure in all directions. A 3D accelerometer can also be used to measure tilt when gravity is the dominating acceleration component (i.e. the sensor is not accelerating very much).

A more precise method for inclination measurement is the use of gyroscopes. They sense the angular rate via different mechanisms, such as spinning rotor, laser, or vibrating mass.

A unit combining three accelerometers (placed orthogonal to each other) and three gyroscopes is called an Inertial Measurement Unit (IMU). It is used to measure the relative inertial movement of the unit. This means it does not measure the location of an object per se, but merely its trajectory from its original location by sensing instantaneous acceleration components and computing the location by double integration. However, this technique can prove inaccurate, as slight errors in acceleration values accumulate resulting in incorrect velocity components which in turn distort the computation of the position. Hence, the accuracy of the measurement declines as a function of measurement duration.

IMUs were primarily developed for the use of aerospace industry to be used in aircrafts (manned and UAVs), spacecrafts (shuttles, satellites and landers) and certain watercrafts such as guided missiles. IMU serves typically as the main component of their inertial navigation systems enabling dead reckoning of the vehicle. However, in recent years these units have spread to various consumer electronic devices as well, ranging from mobile phones to portable media players. In fact, the most widespread motion sensor unit today is probably inside the Wiimote controller of the Nintendo Wii video game system (around 74 million game systems shipped as of June 2010, and a single console is usually equipped with more than one controller). The rapid sprawl of IMUs into consumer electronics has enabled mass production processes in their manufacture, which has subsequently collapsed the prices of the chips. This will most likely breed even more inexpensive applications employing motion sensing. Noninvasive IMU applications do not measure directly the motion of the bones.

Mechanical methods

This class contains methods that are based on measuring mechanical force by various measurement devices. Traditional example for ankle joint motion measuring is a pedal. The downside of these techniques is that they require force and thus create unwanted motion resistance. They also typically do not obtain full 6 degrees of freedom measurements: For example, a pedal records rotation only around a single axis (1 DoF).

Optical methods

Optical methods cover motion capture technologies based on various combinations of active or passive markers and cameras. These are widely used in sports science and in the movie industry to create computer graphics effects and even completely computer-generated characters. A prime example of an extensive use of optical motion capture technologies would be the 2009 hit film Avatar.

Passive markers are external markers that are attached on the subject to be measured. They are made of retroreflective material which reflects back the light that is generated near the camera lens, and the reflected light is collected by the camera. Choosing a suitable intensity threshold and using multiple cameras enables recording of the 3D movement of the markers. Active markers work essentially likewise, but instead of reflecting back external light they emit their own light. Recently, improvements in machine vision and learning have enabled camera systems that work without any markers whatsoever [Corazza et al., 2010].

The weak point of optical methods is the fact that they do not measure directly the bone angles, but merely the movements of markers placed on the skin. Hence, the technique is prone to soft tissue movement errors and not very applicable for our needs. A method to reduce this problem is to attach the markers directly into the bones (by pins or such). Regrettably, the cost for improved accuracy is raised invasiveness.

Medical imaging and comparison between methods

Somewhat less explored area in the field of motion capture is the use of medical imaging methods, such as x-rays/computed tomography, or magnetic resonance. As imaging times of these modalities continue to decrease, the main challenge is shifting from hardware to software development: key area here is working on image segmentation, image registration, and rigid-body kinematics problems. The next chapter will consider further the possibilities of dynamic medical imaging in motion capture problems. Table 1 provides a brief overview of different motion capture techniques.

Table 1: Various motion capture techniques.

method	**accuracy / precision**	**Inva-sive**	**weaknesses / notes**	**hospital ready**
Current mainstream method (visual expert estimation)	Very low	No	not full 6 DoF (only sagittal plane analysis)	Yes
MRI slices, 3D registration	Low-intermediate	No	poor bone contrast	Yes
CT slices, 3D registration	?	No	radiation dose (intermediate)	Yes
X-ray stereophotogrammetry [Kärrholm, 1989]	1 mm [Douglas et al, 2004], 0.5 mm [You et al., 2001]	No	radiation dose (low)	Usually no
Optical stereophotogrammetry /w skin markers [Cappozzo et al., 1996]	Low	No		No
Optical stereophotogrammetry /w bone markers	High	Yes		No
Optical stereophotogrammetry w/o markers	Low	No		No
Mechanical measurement devices (footplates, etc.)		No	measurement affects motion (since requires force), usually not full 6 DoF	Usually no
Coordinate measuring machine (CMM)	Very high (in theory <0.01 mm)	Yes	requires steady fixation of the limb, usually accuracy much lower due to non-rigid fixation [Björkstrand et al., 2010]	No
Inertial measurements	Low	No		No

4.3 Direct vs. indirect motion capture

The distinction between direct and indirect motion capture techniques is defined in this thesis as follows: the direct imaging methods record the relative movements and orientations of individual bones, whereas the indirect methods measure chosen anatomical locations whose motion correlate (to a varying degree) with the actual bone movements. The most prominent example of this is the use of skin markers. The error generated by soft tissue movement artifact can be rather easily even several centimeters, as can be seen in figure 7 (note that the artifact is less severe in ankles). Various algorithms and techniques have been proposed to cater to this problem, but they do not provide enough accuracy yet [Andersen et al., 2010]. According to Peters, the soft tissue artifact on the tibia may be up to 15 mm [Peters et al., 2010].

It is important to note that many established uses of motion capture technologies differ fundamentally from the requirements of joint motion capturing. The techniques used in, say, film industry and sports research (e.g. low to intermediate resolution optical methods) might be called *qualitative* [Godfrey et al., 2008] methods: they usually aim to model merely the visual motion of a body, and thus a centimeter - or even decimeter - scale accuracy is sufficient. In this thesis, a need is for *quantitative* technologies and millimeter-scale accuracy.

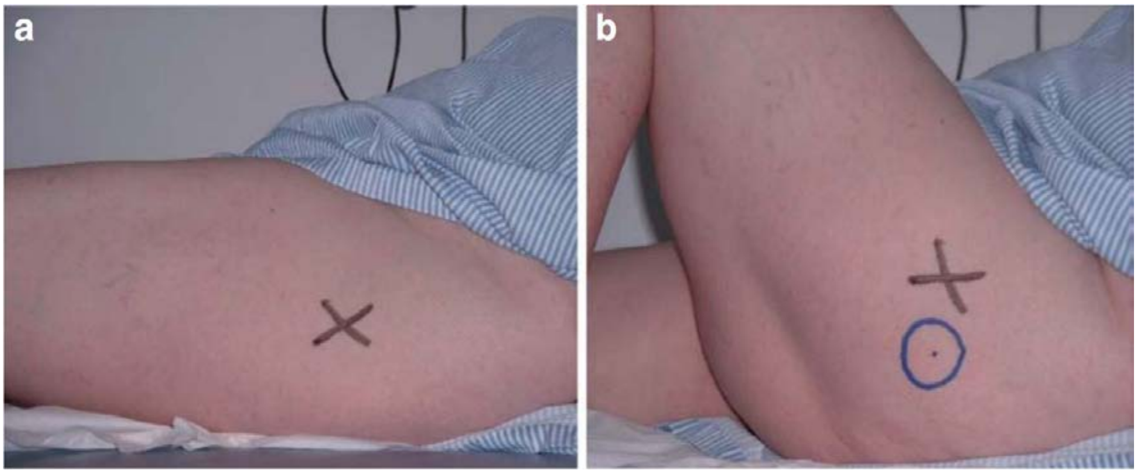

Figure 7: The effect of the soft tissue movement artifact: (a) with the knee in extension, *X* is marked superficial to the greater trochanter, and (b) the knee is flexed and a new “location” (or superficial projection) of the greater trochanter is marked by *O*. The distance between markers *X* and *O* represents the skin movement artifact which can be seen to be in the scale of several centimeters.

4.4 Contralateral joint comparison

Sometimes it is not possible to measure the motion of a certain damaged joint, e.g. due to excessive swelling. This can be circumvented by imaging the opposite joint. In order to successfully estimate the range and the arc of motion of the ipsilateral (injured) ankle by measuring the contralateral (intact) ankle complex, a prerequisite is obviously a sufficient amount of symmetry. According to the studies of Stefanyshyn and Engsberg

[Stefanyshyn and Engsberg, 1994], and Siegler [Siegler et al., 2005] the ranges of ankle motion are not significantly different between the sides. Kozanek and colleagues [Kozanek et al, 2008] concluded that the same applies to the knee joint complex: a ligament injury in ipsilateral knee does not alter the motion of the contralateral knee, thus it can be used as a kinematic control knee in assessing the joint motion.

5 Dynamic and quasi-dynamic medical imaging

5.1 Dynamic medical imaging modalities

The dynamic imaging refers to structural and functional imaging techniques capable of kinematic (motion) imaging, i.e. possessing a high temporal resolution and near video rate scanning possibility. This chapter lists the different principal modalities, and compares their specifications from the viewpoint of their applicability for joint motion study for rapid manufacturing.

The medical imaging modalities currently in widespread clinical use are X-rays/CT, ultrasound, nuclear (or radioisotope-aided), magnetic resonance and optical methods. All of these techniques offer various real-time imaging applications. Nuclear imaging methods include modalities such as PET and SPECT, which are generally used for functional imaging purposes (e.g. flow studies of air and blood flow in brain, thorax etc.). Therefore they are of little use in anatomical joint motion studies. Optical methods (e.g. NIRS or CARS) are not applicable either, since they do not penetrate very deep into organs.

X-rays and computed tomography are the preferred techniques for imaging bones, but give a small to moderate radiation dose to imaged tissues. Magnetic Resonance imaging offers an excellent contrast for soft tissues such as muscles, tendons, and cartilage, and is widely used in joint study. On the other hand, MRI gives a weak signal with bone – CT is preferred to MRI for extra bone details. The main drawback of MRI is however its limited temporal resolution; scanning times are getting shorter year by year, but a generation of a high resolution 3D MR image might easily take several minutes. While fast MRI applications do exist [Uecker et al., 2010] even in joint motion studies [Draper et al., 2008], they usually give a limited accuracy (2 mm in [Draper et al., 2008]). Computed tomography is distinctly faster technique: a full-body scan is completed in range of seconds, and by limiting the scanned area to the joint under study (such as knee, ankle or wrist) and, if needed, the image quality, a real-time (video rate) imaging is possible.

Ultrasound imaging is by far the preferred choice in obstetrics and other soft tissue studies of the abdomen. It is completely safe to the patient and offers real-time imaging (for example circulation velocities by Doppler technique, but also structural studies). It is reasonably applicable for joint soft tissue imaging, but its main limitation is the fact that bones block ultrasound.

For our study, we got an access to a cone-beam CT device that did not achieve real-time imaging times, but temporal resolutions of approximately 20 seconds. This was sufficient for finite helical axis measurements since the patients could hold their ankles still for whole scanning time.

5.2 X-ray and computed tomography

The principle of X-ray imaging is straightforward: A flux of photons is accelerated by an X-ray tube through an object (e.g. a patient, or certain part of patient's body). As electromagnetic radiation, the flux penetrates the object. However, a certain part of the photons react with the atoms in the surrounding medium and are either absorbed or scattered. The rest of the flux exits the object from the opposite side, and is collected by a detector (such as a photographic plate, or a grid of scintillators). The photon counts at different parts of the detector create an intensity profile, which can be compared to the initial, more intense, photon flux from the x-ray tube. For homogeneous medium and monochromatic radiation, the radiation attenuation can be expressed with the Beer-Lambert law [Webb, 1988]:

$$I = I_0 e^{-\mu s} \tag{1}$$

where I_0 is the intensity of the initial radiation, I is the detected flux, s is the distance traveled in the medium, and μ is the linear attenuation coefficient. The linear attenuation coefficient is characteristic to each material or tissue type, and also depends on the used radiation frequency (which determines the energy of the photons). For non-monochromatic radiation and two materials as seen in figure 8, the equation becomes:

$$I = I_0 e^{-\mu_1(E)s_1 - \mu_2(E)s_2} \tag{2}$$

where E denotes the radiation energy.

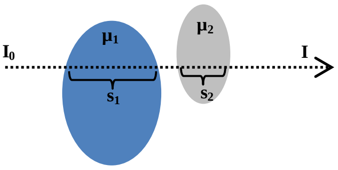

Figure 8: The attenuation of radiation (I_0) after passing two objects of different radiodensities.

As materials with different linear attenuation coefficients are added, the exponent is generalized into a line integral:

$$I = I_0 e^{-\int \mu(E) ds} \tag{3}$$

The radiodensity (i.e. the attenuation coefficient) for bone is relatively high, while for soft tissue and ambient air they are lower. Hence, bone attenuates radiation more per traveled distance. The detected intensity profile creates the radiographic contrast needed to form a planar 2D X-ray image. When multiple X-ray projections taken from different angles are combined, a three-dimensional image can be reconstructed. This is called computed tomography, CT.

Figure 9 illustrates the principle of computed tomography. The object is scanned from several projection angles, yielding multiple intensity profiles on a rotating detector, or multiple detectors: In the figure, the intensity profiles on every detector are bell curve shaped, since the photons passing through the center of the ball pass longer distance in a radiodense substance than the photons passing near the edges of the ball. After acquiring intensity distribution information from each detector, a computer can calculate a model of three-dimensional pixels, or voxels, each with their own linear attenuation coefficient. The summing of different projections at an arbitrary voxel is called an inverse Radon transform, and the whole process of image construction is called backprojection.

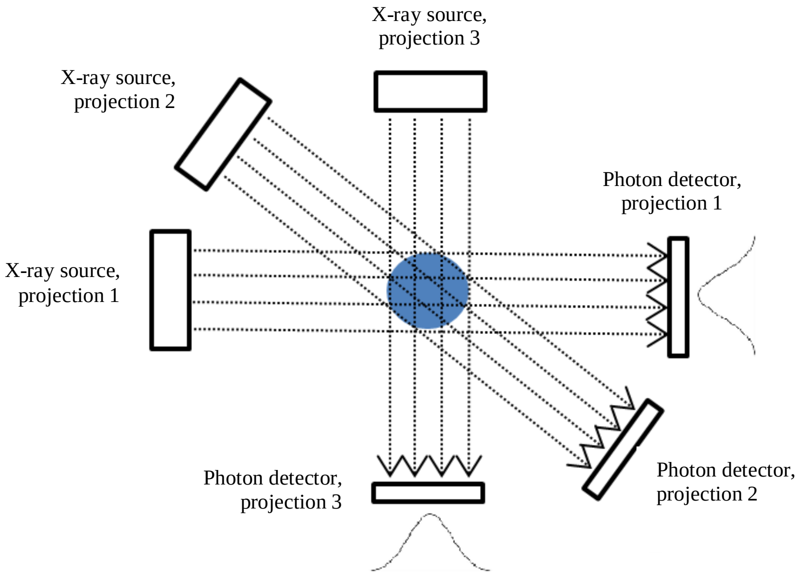

Figure 9: The principle of computed tomography imaging. Planar X-ray images are scanned in several projection angles, and the detectors gather intensity profiles (the bell curves).

Most CT applications do not denote voxel intensity values by raw linear attenuation coefficients (radiodensities). They are usually calibrated in respect with the radiodensity of water (which determines *CT number*), or densities of water and ambient air (*Hounsfield units, HU*). For example, the HU value is defined by:

$$HU = 1000 \times \frac{\mu_0 - \mu_{H_20}}{\mu_{H_20} - \mu_{air}} \quad (4)$$

where μ_0 denotes the “raw” attenuation coefficient of the voxel. μ_{H20} is 0 and μ_{air} is -1000, by definition. Some common Hounsfield values are listed in table 2.

Table 2: Hounsfield values of various tissue types.

Substance	**HU**
air	-1000
fat, soft tissue	-120…-350
water	0
muscle	+40
bone	+400 or more

Typically, X-ray photons are collected with ionization chambers filled with high-pressurized Xenon. High pressure is used to maximize the number of collisions between gas molecules and X-rays.
Medical image quality can be assessed by several quantities, such as spatial resolution and contrast resolution. Spatial resolution denotes the size of the voxels, while contrast resolution denotes the maximum intensity variation between adjacent voxels. Hence, low spatial resolution causes aliasing and low contrast resolution causes blurring. Usually a compromise needs to be made between these (and the radiation dose). This triangular interdependency can usually be approximated by the following relationship:

$$D \propto \frac{SNR^2}{P^3 T} \tag{5}$$

Here D denotes the dose, SNR is the signal-to-noise ratio, and P and T pixel size and slice thickness, respectively. Since the voxels are isotropic, the formula simplifies into:

$$D \propto \frac{SNR^2}{P^4} \tag{6}$$

CT imaging of bones yields a high natural contrast which permits to chase high spatial resolutions. They can be achieved by e.g. utilizing “sharp” bone-type reconstruction kernel (reconstruction algorithm with high spatial frequency). When imaging lower contrast details, such as soft tissue, sharp kernel creates too much noise which fades the pursued details.

According to the current European Union regulations [European Council, 1997], the radiation dose imposed to the patient and the personnel needs to be minimized to the lowest amount that is clinically acceptable. This limits both the contrast resolution and the spatial resolution according to the equation 6.

5.3 Cone-beam computed tomography (CBCT)

Cone-beam computed tomography is a recent technique which has already gained wide use in dental medicine. Instead of linearly collimated one-dimensional detector row (or multiple rows) like the one used in traditional fan-beam CT devices, a two-dimensional detector array is employed. This allows a significant reduction of the imposed radiation dose without compromising the image quality, because collimation always loses information (major part of the photons end up in the collimating structures instead of detectors, even though they have contributed to the radiation dose).

Cone-beam CT allows high resolution with moderately low radiation doses. On the other hand, the increased non-linearity of the backprojection process raises the computational complexity of the problem.

5.4 Image segmentation

Image segmentation refers to a problem of partitioning a digital image into multiple segments (masks, or homogenous sets of voxels): in medical image analysis this segment could be for example an organ, body part or other region of interest (ROI). For experienced human eye this is usually relatively simple – albeit possibly time-consuming – task, but the transfer of the ability to computers is much less straightforward. Thus, a wide variety of algorithms have been developed, each with their strengths and weaknesses. Some of the most common-used methods include:

- level methods
- region-based algorithms
- edge-based algorithms
- feature-based algorithms

Level methods (intensity thresholding)
This is perhaps the simplest of available segmentation methods. An algorithm analyses image voxels one by one, adding them into the active mask subset in case their intensity value exceeds and/or falls below designated preset threshold values. Subsequently, image noise can be reduced by filtering out islands with smallest radii.

Region-based algorithms
A point or voxel in the ROI is selected, either manually or automatically – this is called the seed point – alongside a threshold intensity value. After this, the algorithm starts to expand the segmented region by comparing the intensities in neighboring voxels to the threshold value. This algorithm is repeated iteratively until whole of the ROI is segmented. Hence, region-based algorithms are somewhat analogous to the flood-fill tools in typical graphics editing software.

Edge-based algorithms
This class covers the methods which are based on the recognition of edges and surfaces in an image. This can be done either in two dimensions to the image data (slices) or in three dimensions after a CAD (computer assisted design) model of the image is created.

Feature-based algorithms
This type is based on the detection of distinct features in the image by comparison with a pre-defined atlas of features, such as a collection of predefined bone shapes.

5.5 Image registration

Image registration refers to the process aiming to bring two or more medical images in different frames of reference into a common coordinate system, for example in order to align them as layers and merge into a single picture. The images might be acquired at separate times, or with various imaging modalities (multimodal applications aim to combine the strengths of multiple imaging methods).

Available tools in image registration are three kinds of transforms: translation (moving), rotation, and scaling. These are called rigid transformations, since they do not alter the shape of the object. In bone registration tasks these usually suffice, since bones are not very elastic by nature. Figure 10 clarifies the types of image transforms available [Maintz and Viergever, 1998]. Global transformations refer to transforms affecting the whole image, whereas local transformations transform only a part of the image, or whole image but with different parameters for separate parts.

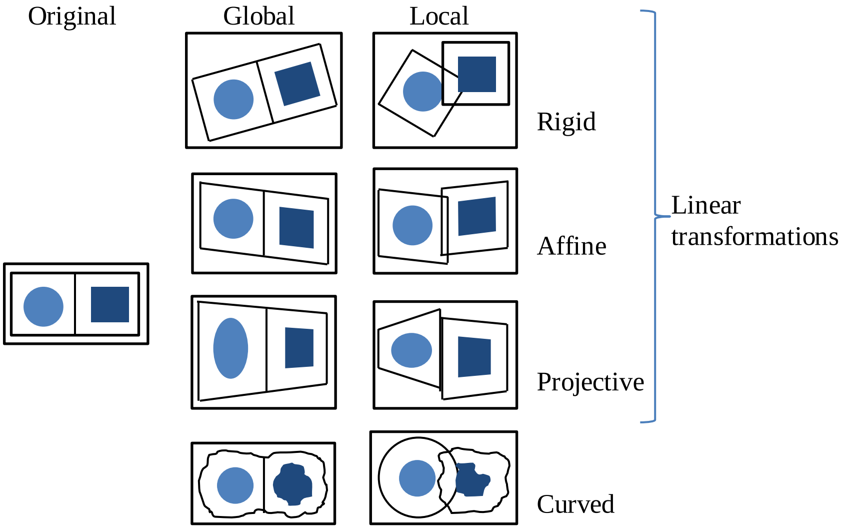

Figure 10: Image transformation types.

When these separate sub-transforms are combined, one gets a single registration transform. In order to acquire this, the relative difference of the coordinate systems needs to be computed. Various methods and algorithms exist for the registration transform computing problem. These are usually based on one of the following techniques:

- external markers
- internal markers (landmark based)
- atoning of the counter-surfaces
- intensity values of the image (voxel property based)

External or internal markers
A few (typically 3-15) spatially corresponding points are either known or defined (internal markers), or attached (external markers) in each image, and these point sets are aligned with each other by e.g. square sum minimization.

Atoning of counter-surfaces or intensity values of the image
The correspondence of the surface points or intensity values of the voxels is maximized iteratively. In this thesis, a segmentation matching algorithm is used since tibia and talus do not contain any distinct or pointy features where we could have attached a marker.

6 Materials and methods

6.1 Case study description

Figure 11 presents the proposed ankle fracture treatment flow. In the figure, phases covered in this thesis are marked: CT scans in several stances, image segmentation, image registration (manual and automatic), and the calculations of the rotation axes.

As a case study, the ankles of two voluntary patients were modeled. In the absence of a traumatized ankle, healthy ankles had to be used. A badly shattered shinbone (tibia) might potentially complicate the image segmentation and registration tasks. The subjects were both male, aged 45 (subject 1) and 26 (subject 2), both without histories of severe ankle fractures.

The device used was a cone-beam limb CT scanner by Planmeca, which was in its prototype phase. The measurements served at the same time as an operation test for the new device. The CT scanner offered a promising voxel size of 0.4 mm (0.2 mm after computational reconstruction). The voxels were isotropic, i.e. evenly dimensioned in every direction – in other words, the slice thickness equaled the voxel size.

The ankle of subject 1 was imaged in three stances: neutral, full dorsiflexion, and full plantarflexion. Measured motion was unloaded active motion. Subject 2 was imaged five times: in aforementioned stances, and additionally, half dorsiflexion and half plantarflexion.

Figure 12 shows three CT image slices from the dataset. Figure 12a is the axial view, with the tibia and the fibula visible. Figure 12b displays a coronal view, with the tibia on the top and talus the bone in the middle. Figure 12c is a sagittal view.

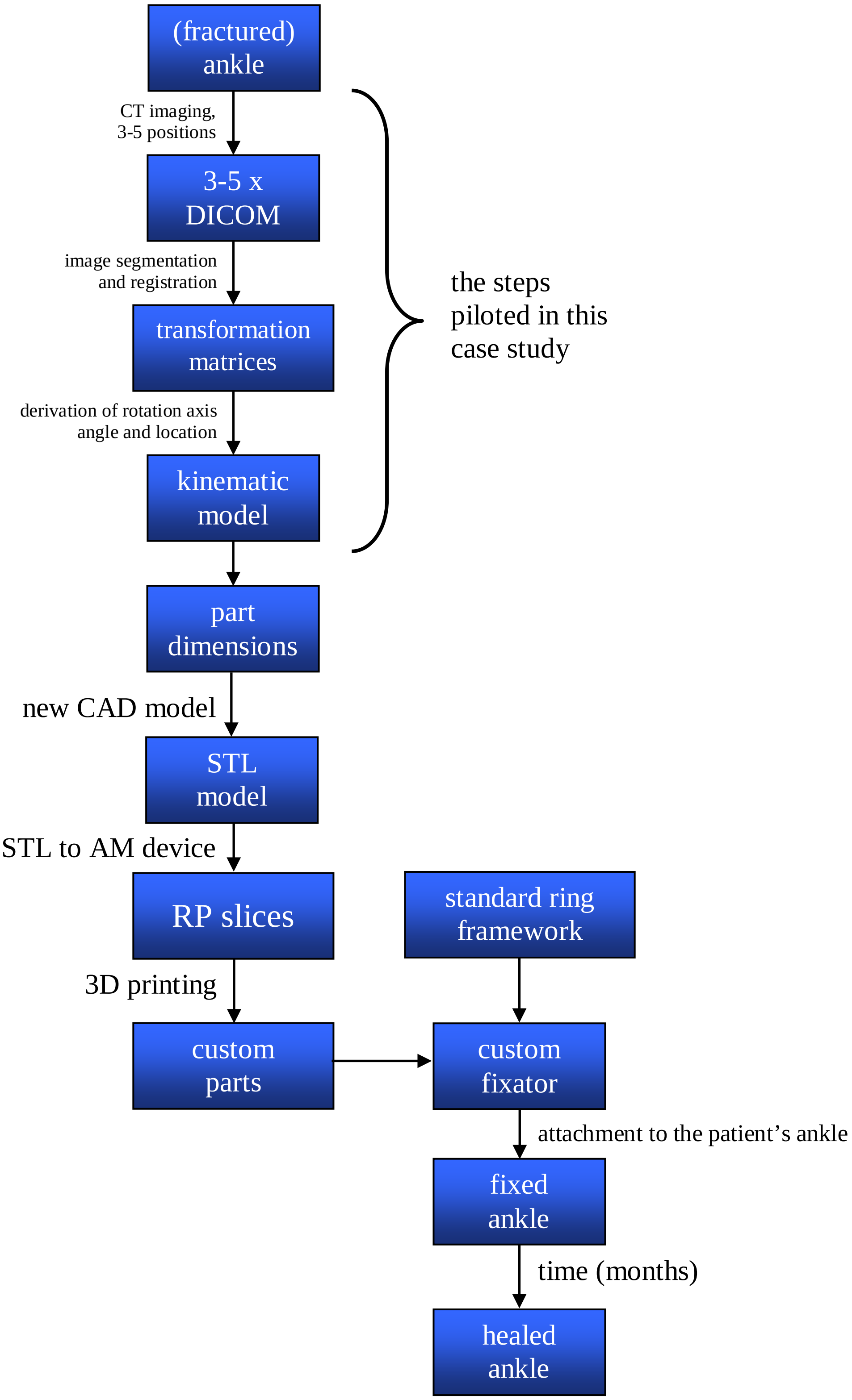

Figure 11: The proposed treatment flow for ankle fracture, and phases described in this thesis.

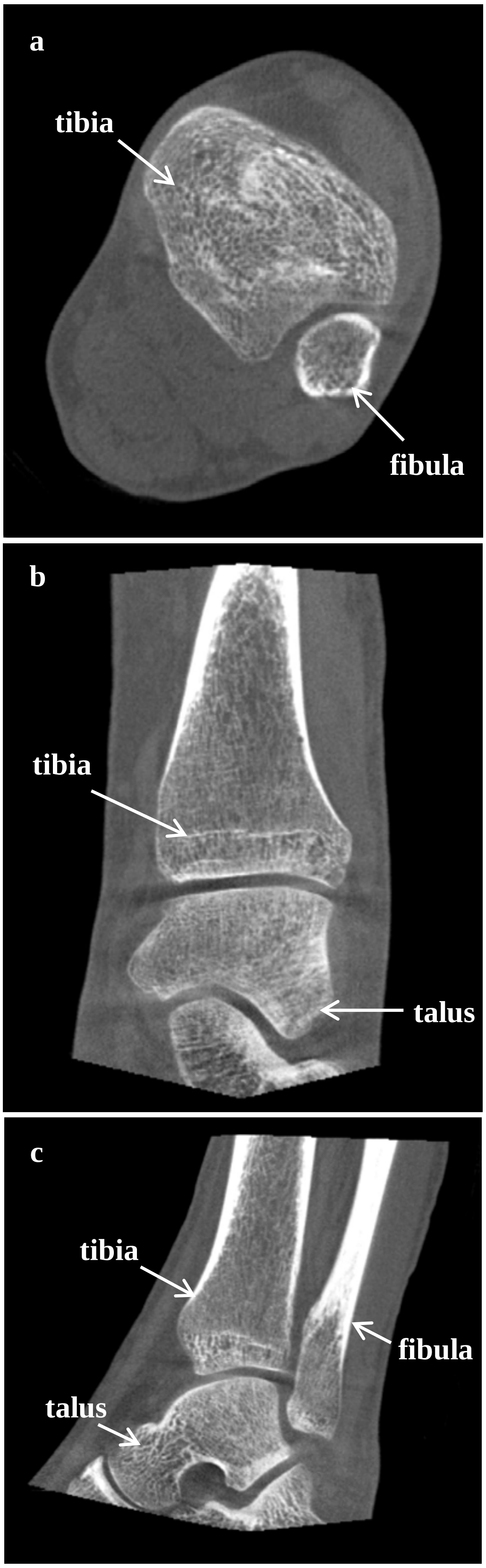

Figure 12: Computed tomography image of the patient’s ankle. (a) Axial view. (b) Coronal view. (c) Sagittal view.

6.2 Methodology

The Dicom image sets were initially opened, segmented and viewed with 3D Slicerversion 3.6 (open source software platform for visualization and (medical) image analysis available at www.slicer.org) [Gering et al., 1999], [Pieper et al., 2004], [Pieper et al., 2006]. The segmentation software was soon changed into Mango (Multi-image Analysis GUI, by Jack L. Lancaster, Ph. D. and Michael J. Martinez), since it was considerably more stable and required less manual correction of segmentation. The tibia and talus bones of each image were segmented – more of this process is described in the "Results" chapter.

3D Slicer was continued to be used for 3D model rendering, and for the first actual post-CT step of the process: initial image registration. This was done manually, i.e. by using transform types described in chapter 5.5 (except no scaling was performed, since the bones can be assumed to retain their shape), the moving image was guided to correspond to the fixed image. More specifically, the registration was done several times: for each image pair, there was one registration for the tibia, and one registration for the talus. Manual (and automatic) registration in two dimensions is trivial, but in three dimensions it can be cumbersome – there are six degrees of freedom (three rotations combined with three translations), and altering one of them to correct the registration in one slice will disarray all the other slices. For this reason, the manual registration in 3D Slicer was performed only in rough detail: in all 6 degrees of freedom, a deviation of around 1° (angles) or 1 mm (translations) from spot-on registration was allowed – this would be merely an initial registration for an automatic registration algorithm.

Figures 13-20 demonstrate the two registrations that were performed for each FHA which was to be calculated. Figures 13 and 14 show first a tibia in a neutral stance and a half dorsiflexed stance before their registration. Then, figures 15 and 16 present the registration results: the targeted bones are overlaid in the two images. Similarly, figures 17-20 demonstrate the same process with the talus bone.

Figure 13: Tibia in neutral stance before registration.

Figure 14: Tibia in half dorsiflexed stance before registration.

Figure 15: Tibia in half dorsiflexed stance after registration into the neutral coordinate system.

Figure 16: Half dorsiflexed and neutral stances registered and overlaid with a 50/50 alpha blend. Notice how the tali and calcanei do not correspond in the images, whereas the tibias do (to a certain accuracy).

Figure 17: Talus in neutral stance before registration.

Figure 18: Talus in half dorsiflexed stance before registration.

Figure 19: Talus in half dorsiflexed stance after registration into the neutral coordinate system.

Figure 20: Neutral and half dorsiflexed stances overlaid with alpha blend.

After the segmentation (in Mango) and initial registration (in 3D Slicer), the segments were registered again with command line controlled Image Registration Toolkit (under license from Ixico Ltd.), and its rigid registration algorithm [Studholme et al., 1999]. Resulting transformation matrices were analyzed in MATLAB 2010b (MathWorks Inc.), and after this, the final axis coordinates were analyzed in Solidworks 2010 CAD suite (by Dassaulte Systemes).

The nomenclature used is as follows: of non-neutral ankle positions, 100% dorsiflexion is denoted either *Do* or *FDo*, and 50% dorsiflexion is denoted *HDo*. Accordingly, *HPl* and *FPl* (or *Pl*) correspond to 50% plantarflexion and 100% plantarflexion, respectively. It is important to note that these percentages are merely indicative, since they were decided by the subject himself: 100% was the extreme position in which the subject could rotate his ankle, neutral was the position in rest, and 50% was the position *approximately* in between these.

The process was done twice. First time, the “reference position”, i.e. the coordinate system in which the other positions were registered, was the neutral ankle position (neutral). The image registration process was performed again using different reference position, this time HDo. Now, instead of registrations “HDo to N”, “HPl to N”, “FDo to N”, and “FPl to N”, the registrations were “N to HDo” and “FDo to HDo”. These results were compared with the original results, serving as a sanity check and a measure of robustness of the registration and axis calculation phase of the process. In other words, performing the registration across different image pairs should yield approximately homogenous results if the primary source of uncertainty lied in previous steps of the whole process – that is, in the medical imaging phase.

6.3 Transformation matrix algebra

After segmenting the Dicom images in Mango, the segmented images were registered by the rigid registration algorithm of IRTK, Image Registration Toolkit command line tool. The used command line parameters are presented in the appendix A. Each registration produced a transform matrix $\mathbf{T}_i$.

$$T_i = \begin{bmatrix} R_{i,11} & R_{i,12} & R_{i,13} & t_{i,x} \\ R_{i,21} & R_{i,22} & R_{i,23} & t_{i,y} \\ R_{i,31} & R_{i,32} & R_{i,33} & t_{i,z} \\ 0 & 0 & 0 & 1 \end{bmatrix}$$

which can be also expressed as a matrix product of the rotation and the effective translation matrices, $\mathbf{T}_i=\mathbf{t}_{eff,i}\mathbf{R}_i$, where

$$R_i = \begin{bmatrix} R_{i,11} & R_{i,12} & R_{i,13} & 0 \\ R_{i,21} & R_{i,22} & R_{i,23} & 0 \\ R_{i,31} & R_{i,32} & R_{i,33} & 0 \\ 0 & 0 & 0 & 1 \end{bmatrix}$$

$$t_{eff,i} = \begin{bmatrix} 1 & 0 & 0 & t_{i,x} \\ 0 & 1 & 0 & t_{i,y} \\ 0 & 0 & 1 & t_{i,z} \\ 0 & 0 & 0 & 1 \end{bmatrix}$$

The matrix multiplication is defined by:

$$(AB)_{i,j} = \Sigma A_{i,k} B_{k,j}$$

We do not yet know the exact hinge point of the transform – the registration origin is an arbitrary voxel, in most algorithms voxel [0, 0, 0], but the anatomical joint center point is most likely located elsewhere. To obtain its relative location, we may rewrite the transformation $\mathbf{T}_i$ as

$$T_i = OR_i O^{-1} C \qquad (7)$$

Here **C** is the translation between the anatomical joint centers of the two images. **O** denotes the translation from this joint center to the origin of the used registration algorithm (e.g. aforementioned [0, 0, 0]), and $\mathbf{O}^{-1}$ is the inverse of this (that is, the translation from the origin to the joint centerpoint).

Using the equation 7, the translation components of **T** can be explicitly presented as:

$$t_{i,x} = \mathrm{R}_{i,11} C_x + \mathrm{R}_{i,12} \mathrm{C}_y + \mathrm{R}_{i,13} C_z + (\mathrm{R}_{i,11} - 1) O_x + \mathrm{R}_{i,12} O_y + \mathrm{R}_{i,13} O_z \qquad (8a)$$

$$t_{i,y} = \mathrm{R}_{i,21} C_x + \mathrm{R}_{i,22} \mathrm{C}_y + \mathrm{R}_{i,23} C_z + \mathrm{R}_{i,21} O_x + (\mathrm{R}_{i,22} - 1) O_y + \mathrm{R}_{i,23} O_z \qquad (8b)$$

$$t_{i,z} = \mathrm{R}_{i,31} C_x + \mathrm{R}_{i,32} \mathrm{C}_y + \mathrm{R}_{i,33} C_z + \mathrm{R}_{i,31} O_x + \mathrm{R}_{i,32} O_y + (\mathrm{R}_{i,33} - 1) O_z \qquad (8c)$$

Since we have previously obtained two transformation matrices ($\mathbf{T}_{tibia}$ = tibia registration and $\mathbf{T}_{talus}$ = talus registration), we obtain in total six equations (the components of both $\mathbf{t}_{eff,tibia}$ and $\mathbf{t}_{eff,talus}$) with six unknown variables (the components of **O** and **C**). The **O** and **C** vectors are identical in both registration transforms, because only two images were registered and a global reference frame was used. $\mathbf{R}_{tibia}$ and $\mathbf{R}_{talus}$ are naturally distinct. The unknown variables were solved as a system of linear equations in MATLAB 2010b.

However, the vectors **O** or **C** do not denote a single joint centerpoint (relative to the origin, or the anatomical hinge point of the moving image, respectively). Instead, the solution space is an infinite locus of axis points. The number of degrees of freedom can be reduced to force the system to converge into a certain solution (one might for example lock $\mathbf{O}_x$ to certain value to achieve an overdetermined system with five unknown variables). Figure 21 illustrates the concept: the trapezoids represent tibias in two images and the triangles represent tali. The fixed “images” are marked with solid line, whereas the moving images are marked with dashed line. The green arrows are the known transformation matrices (for tibia and talus), and the blue lines represent theoretical joint axes. Each point in the centerline of the moving image should be mapped to the centerline of the fixed image by both transforms ($\mathbf{T}_{tibia}$ and $\mathbf{T}_{talus}$).

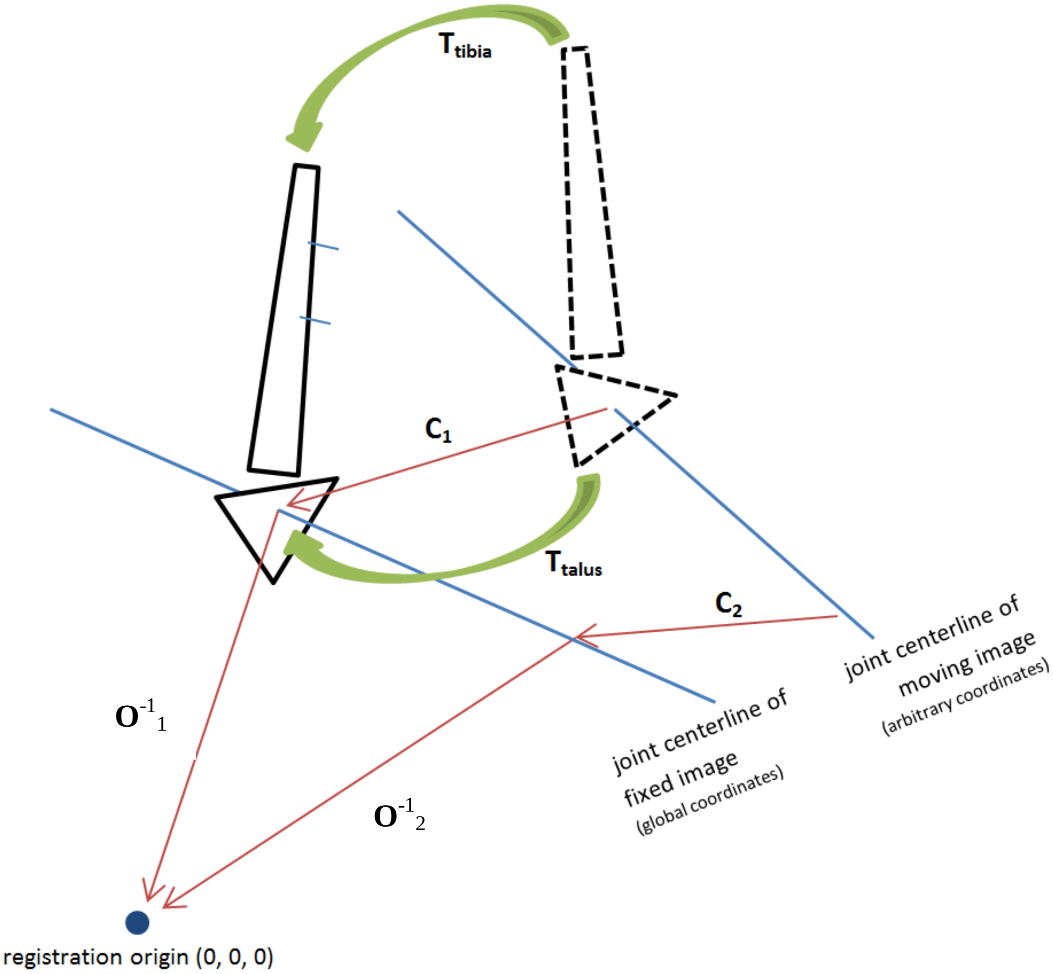

Figure 21: FHA change between two poses (images). The trapezoids represent tibia, and the triangles represent the talus. The blue lines are joint centerlines.

7 Results

7.1 Segmentation results

The segmentation of tibia and talus from each image was performed first. For this task, Mango (Multi-image Analysis GUI) Dicom viewer was used. The segmentation type was a level-set region of interest (ROI) thresholding at -275.0 CT numbers. This value does not correspond to the typical bone radiodensity range in Hounsfield units (300+ HU), since the CT numbers were apparently not calibrated to the Hounsfield scale in the images. Instead, a subjective estimation was used by iteratively searching for an optimum value which would maintain the maximum amount of trabecular bone, but not introduce too much ripple from the cartilage, etc.

Since most of the trabecular bone is located in inside layers of the bones, with cortical bone surrounding it, the ROI thresholding was performed with a shrink wrapping option, which attempts to detect closed regions and fill their insides (like a concave hull algorithm). The wrapping can be done in axial, sagittal, coronal, or 3D directions. The 3D shrink wrapping would be optimal for our purpose, but the algorithm was too unstable to use. Instead, the thresholding was done three times in each plane (axial, sagittal, and coronal). Each operation added trabecular bone voxels to the segmented ROI, and the end results were satisfactorily close to filled bones (albeit not perfect, as can be seen later). Figure 22a shows the CT images of bones in Mango prior to the segmentation, and figure 22b shows the end results.

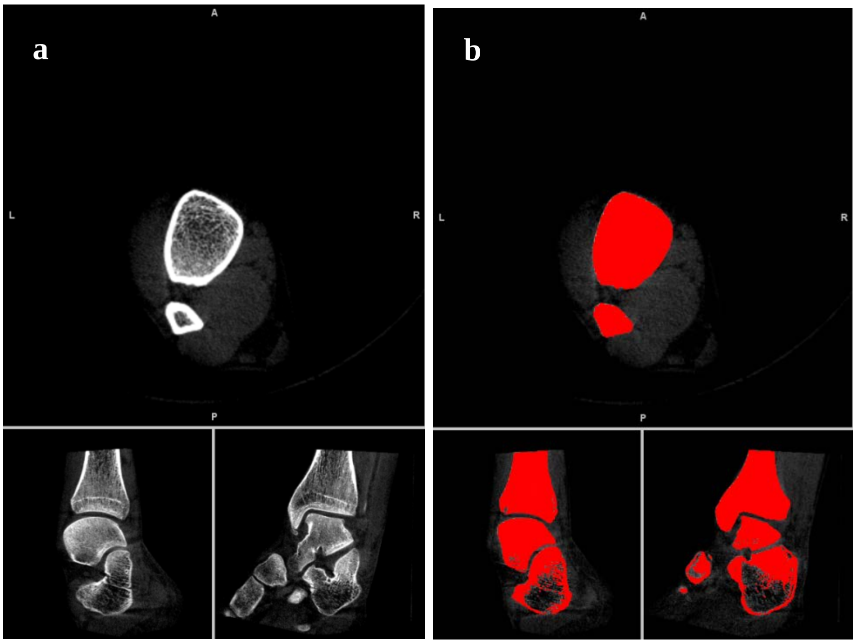

Figure 22: The ankle joint complex before (a) and after (b) segmentation in Mango. Top: axial view. Bottom left: coronal view. Bottom right: sagittal view.

Subsequently, the tibia and talus need to be separated into their own regions. This is done semiautomatically by a ROI preservation algorithm, which asks a seed voxel (an arbitrary voxel in tibia or talus), and starts to grow a new region until it reaches the outer limits of the ROI (bone layer). The bones after separation can be seen in figure 23, with the tibia marked bright green, and the talus red. The rest of the bones (calcaneus and fibula, etc.) are left white.

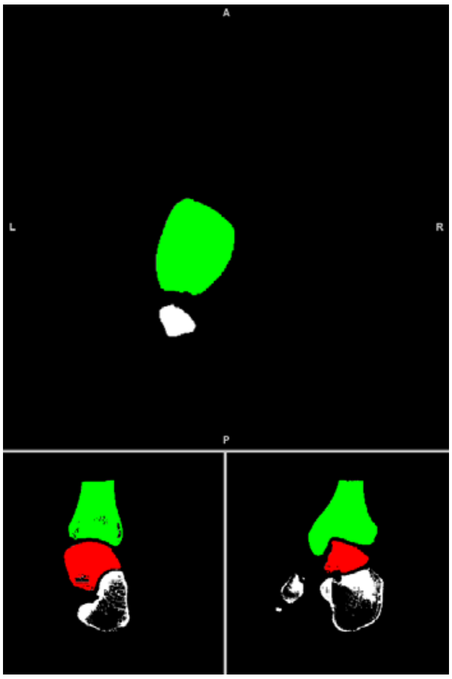

Figure 23: The segmented bones separated by region recognition algorithm. The green bone is tibia and red bone is talus. Rest of the bones are white. Top: axial view. Bottom left: coronal view. Bottom right: sagittal view.

For visual result validation purposes, the two ROIs (tibia and talus) were saved as NIFTI volume files, and imported into 3D Slicer in order to perform 3D rendering. Figure 24a shows the 3D models of the bones (blue is tibia, green is talus). The rendering (or model making, as Slicer refers to it) was executed with no smoothing or decimation iterations. Figure 24b presents the talus from side angle. Notice the missing bone especially in the neck of the talus. This deficiency is rather difficult to correct, without excessive manual labor. The segmentation could have been done with lowered local threshold value in the talus area, but this results in too much noise, such as talonavicular cartilage compounding to the segment. During the course of the project, several images were cleaned manually (i.e. voxel-by-voxel paintbrush operations), but in the end, this was deemed to be too cumbersome. The semiautomatic segmentation results were considered adequate when there are several images to process.

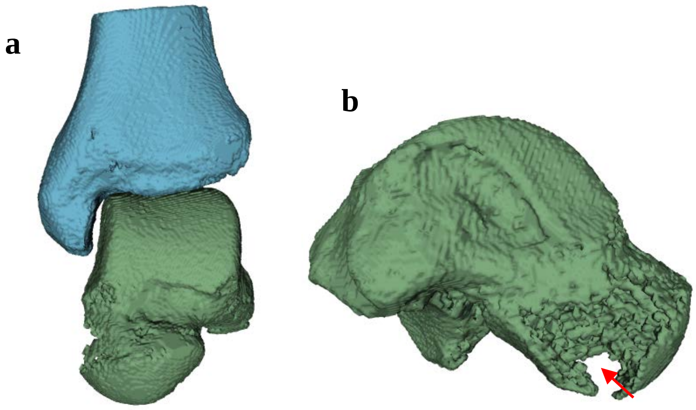

Figure 24: (a) The 3D rendered models of tibia and talus. The models are separate, but inserted into correct coordinate space in their anatomical locations. (b) Side view of the segmented and rendered talus. Notice missing bone especially in the talar neck (red arrow).

At this stage, verification was performed to prove that no serious errors were made thus far, especially that the coordinate systems of the separate tibia and talus files were consistent with that of the initial Dicom image volume. For this purpose, a simple volume render (threshold at -275.0 CT numbers) of the whole image was done in 3D Slicer, and the segmented tibia and talus models were overlaid in it. Figure 25 shows the results: the tibia and talus are located where they should be, i.e. the coordinates were maintained between Mango and Slicer as expected.

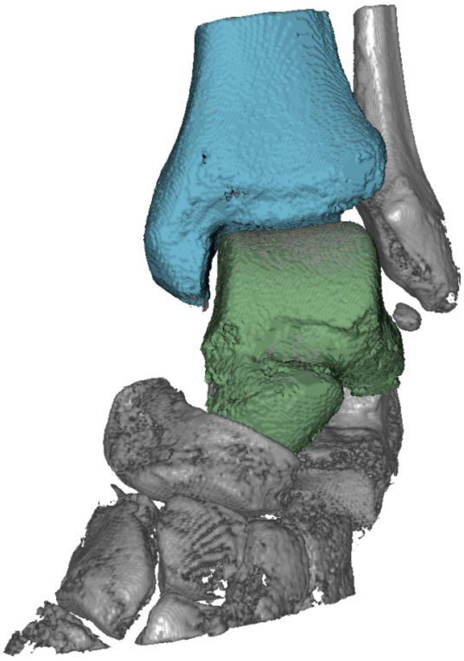

Figure 25: The tibia and talus models overlaid with volume rendering of whole Dicom image (all bones). The models are in correct positions, i.e. the models maintained their coordinate systems.

7.2 Registration results

The ankle of patient 1 was imaged in three stances (neutral, full dorsiflexion, and full plantarflexion). The tibia and the talus were registered separately; hence four registrations were performed in 3D Slicer and Mango/IRTK. The resulting matrices are given below. The 3x3 sub-matrix consisting of three first rows and columns describes the rotation, and the fourth column describes the translation components (t_x, t_y, t_z) in millimeters. The fourth row ([0 0 0 1]) is defined to allow matrix multiplication.

Full dorsiflexion (Do) to neutral (N)

Tibia

0.9998	-0.0049	-0.0201	-0.2979
0.0057	0.9991	0.0411	-3.4500
0.0199	-0.0412	0.9990	-3.7000
0	0	0	1

Talus

0.9756	0.0707	-0.2081	9.0196
-0.0152	0.9663	0.2570	-14.2520
0.2192	-0.2475	0.9438	-0.5608
0	0	0	1

Neutral to full plantarflexion (Pl)

Tibia

0.9990	0.0053	-0.0448	6.4000
-0.0019	0.9972	0.0742	-11.6200
0.0451	-0.0740	0.9962	0.9618
0	0	0	1

Talus

0.9833	-0.0225	0.1803	-2.9000
0.0492	0.9882	-0.1450	-2.0000
-0.1749	0.1515	0.9729	-2.6840
0	0	0	1

The transformation matrices of the patient 2 defined in a similar fashion can be found in the appendix 2.

7.3 Joint axis calculations, subject 1

Figures 26, 27 and 28 present the results of segmentation, registration, and axis calculation of finite helical axes of patient 1’s talocrural joint. The blue line shows the FHA between dorsiflexed and neutral stance, and the black line shows the joint axis between neutral and plantarflexed stance. In addition, the red line shows approximately the location of the common literature reference axis: an axis which passes the distal tips of lateral and medial malleolus.

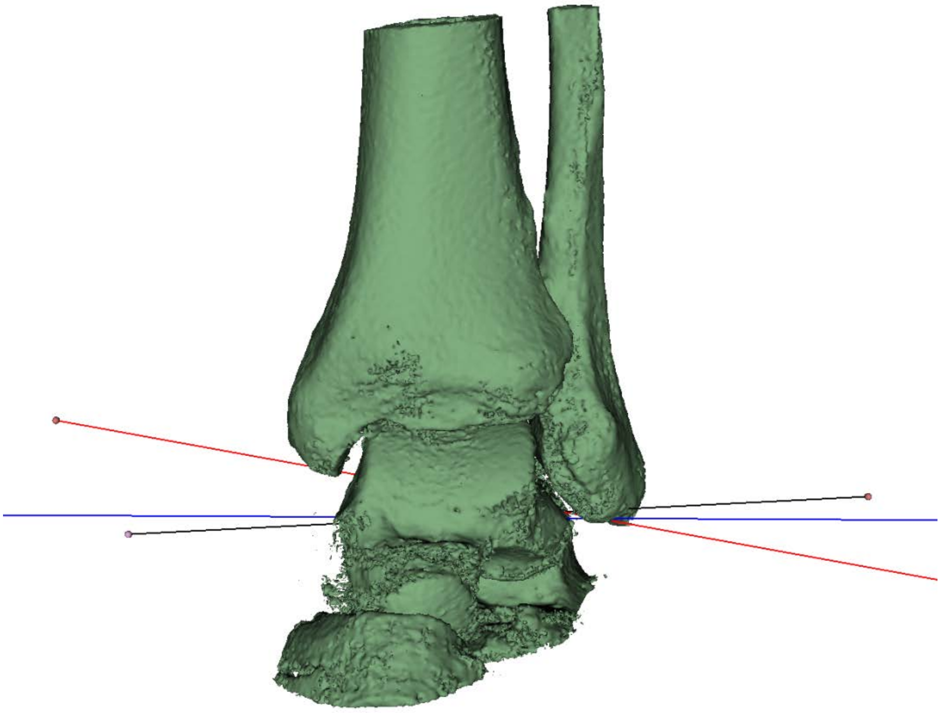

Figure 26: The finite helical axes of patient 1. Red is literature reference axis, blue is Do-N, and black is N-Pl. Coronal (anterior) view.

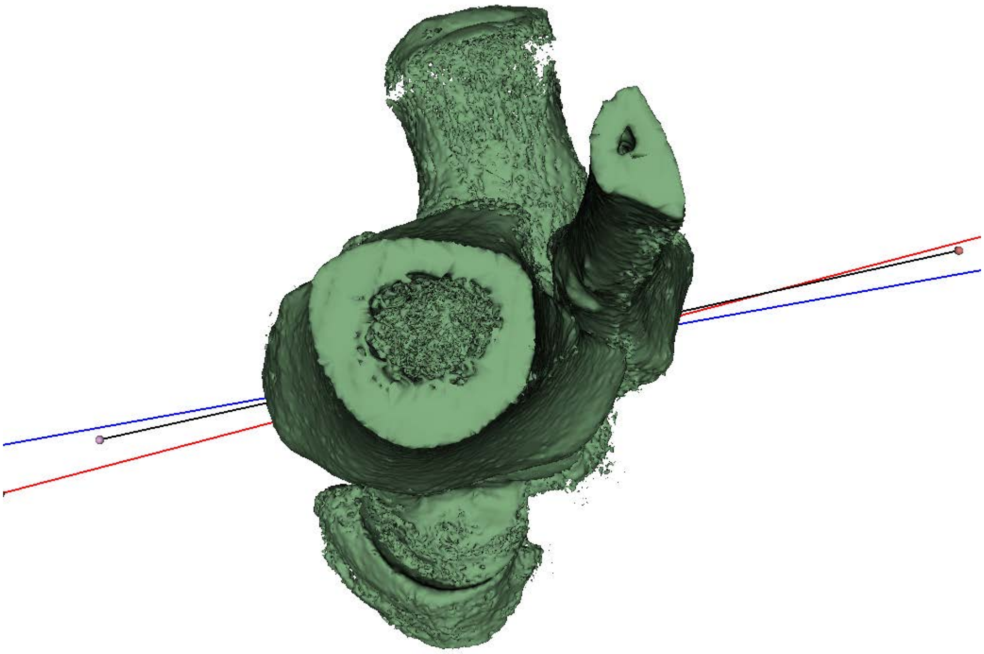

Figure 27: The finite helical axes of patient 1. Red is literature reference axis, blue is Do-N, and black is N-Pl. Axial (superior) view.

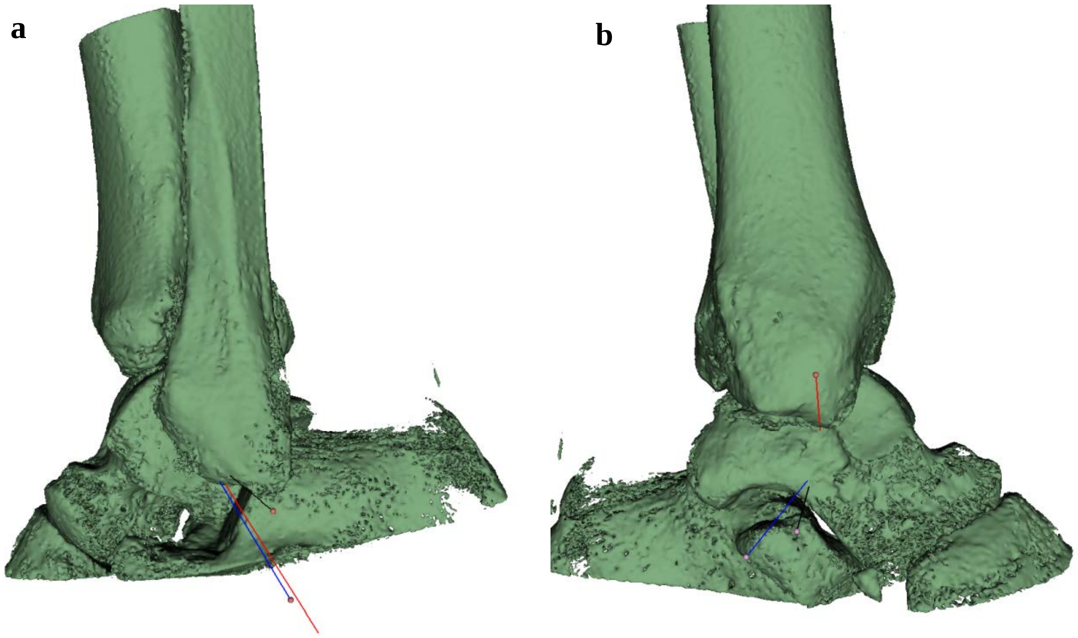

Figure 28: The finite helical axes of patient 1. Red is literature reference axis, blue is Do-N, and black is N-Pl. (a) Lateral view and (b) medial view.

Table 3 presents the change in the orientation of two consecutive FHAs (total axis turn), as well as a comparison between the determined value and approximate literature reference axis (the axis between tips of the malleolus). The results are in absolute values. However, the orientation change is also decomposed into coronal and axial components which carry a sign obeying the right-hand rule: anteroposterior (AP) axis runs from anterior to posterior (i.e. from the toes towards the heel), hence from anterior view, counterclockwise rotations are marked negative. Inferior-superior (IS) axis runs upward. The directions are defined by estimation, with the IS axis running along the tibia and AP orthogonal to it. The majority of the changes seem to happen in the coronal plane.

In addition, the shortest distance between the two axes is calculated perpendicularly. This does not equal to the exact translation amount of the axis, which would indeed be very valuable information, but cannot be determined more accurately with this method since the rotation hinge points of the axes are unknown. However, the reported values serve as a viable lower limit of the true translation – they represent the amount of translation present if the rotations happened about points as close to the other axis as possible. Since in reality, they were likely to happen about another points further away from each other, the real translations can be assumed to exceed reported minimum values.

The last two columns of the table denote the distances between two FHAs measured on the lateral and medial surfaces of the talus. As can be seen, most of the axis distances are relatively small (<2 millimeters), except the literature reference axis which is located much higher than the measured axes in the medial side (10.1 mm and 10.9 mm) – on lateral side, the shift is only 1.3 or 1.6 mm. The talus widths between axis and talar surface intersections were measured, and reported in table 4.

Table 3: Axis orientation and location comparison between consecutive stances and literature reference (subject 1).

	total axis turn (|°|)	**coronal AP turn (°)**	**axial IS turn (°)**	**min translation (mm)**	**axis distance on medial talar surface (mm)**	**axis distance on lateral talar surface (mm)**
Do-N / N-Pl	3.5	-3.77	1.95	0.57	1.3	1.8
lit. / Do-N	12.67	-9.79	-4.88	0.72	10.1	1.3
lit. / N-Pl	15.21	-13.01	-2.43	0.83	10.9	1.6

Table 4: Subject 1's axis lengths inside talus.

	axis length between talar surfaces (mm)
lit. reference	41.6
Do-N	42.6
N-Pl	42.1

7.4 Joint axis calculations, subject 2

The subject 2 was measured alike the first subject. In addition to the neutral (N), fully dorsiflexed (FDo), and fully plantarflexed (FPl) stances, the subject was measured also in half-dorsiflexed (HDo) and half plantarflexed (HPl) stances. As before, figures 29, 30 and 31 show the measured talocrural joint axes and a literature reference axis from three views.

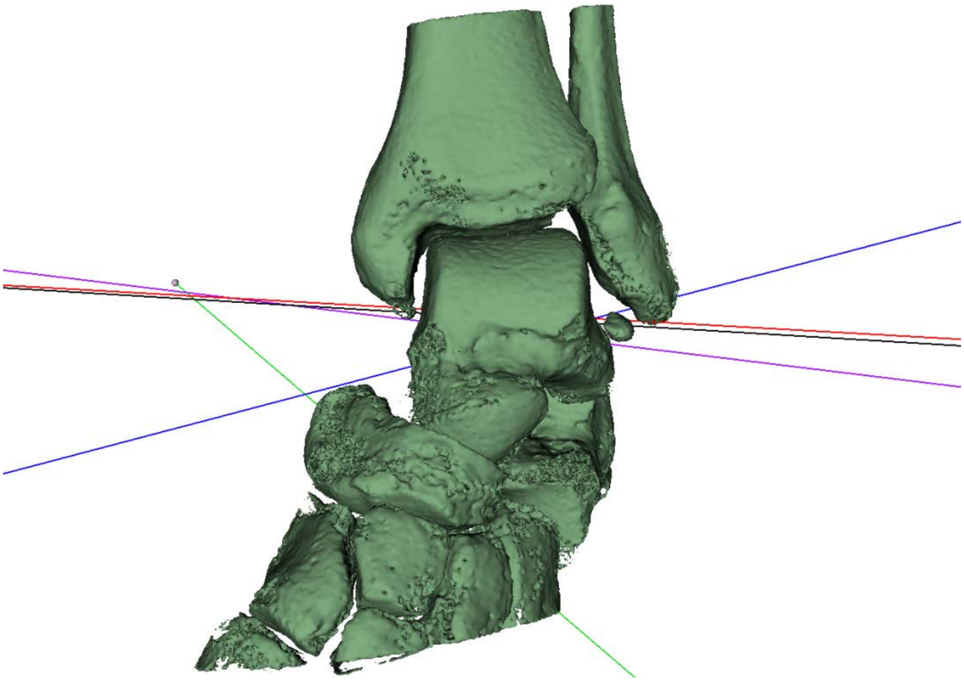

Figure 29: The finite helical axes of patient 2. Red is literature reference axis, purple is FDo-HDo, blue is HDo-N, black is N-HPl, and green is HPl-FPl. Coronal (anterior) view.

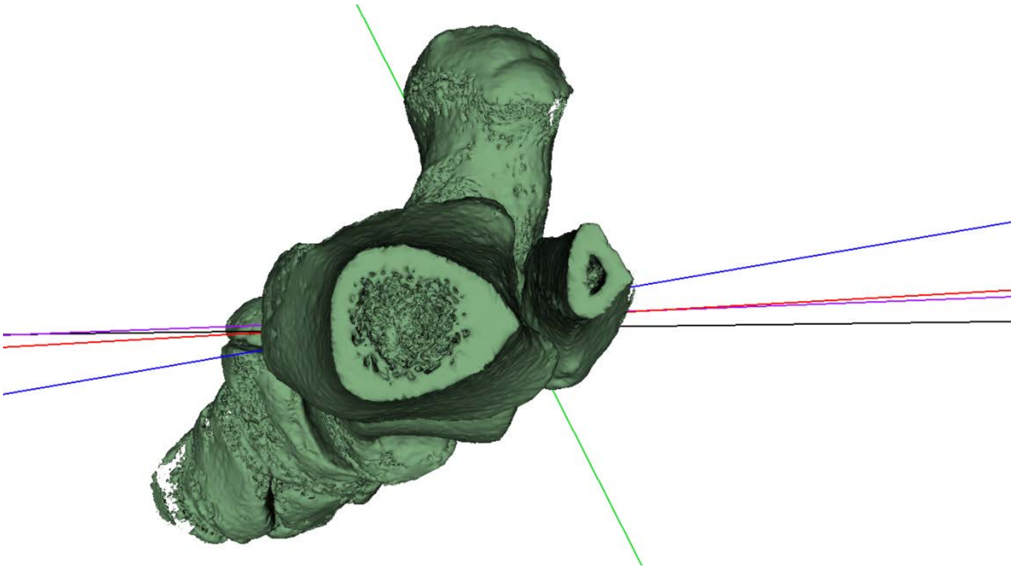

Figure 30: The finite helical axes of patient 2. Red is literature reference axis, purple is FDo-HDo, blue is HDo-N, black is N-HPl, and green is HPl-FPl. Axial (superior) view.

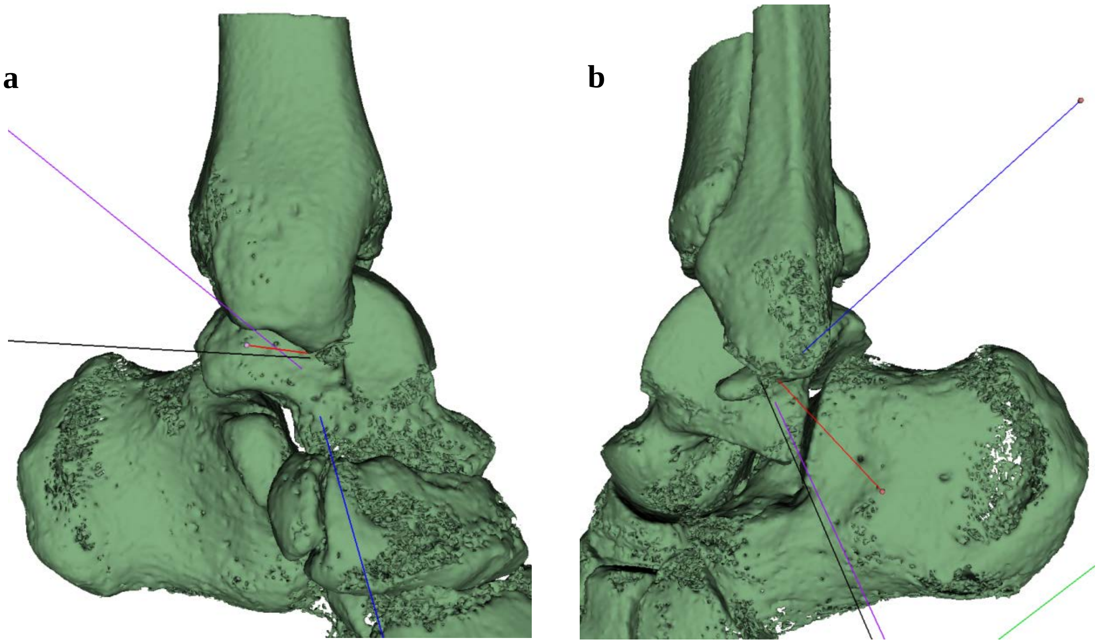

Figure 31: The finite helical axes of patient 2. Red is literature reference axis, purple is FDo-HDo, blue is HDo-N, black is N-HPl, and green is HPl-FPl. (a) Medial view and (b) lateral view.

The finite helical axis between half plantarflexion (HPl) and full plantarflexion (FPl) – the green line – is located in rather abrupt position and orientation. The reason for this was quite apparent in the CT scans: the subject had twisted his ankle much further than 50% of his normal range of motion in the HPl stance – in fact, it was relatively close to the FPl stance. The subject himself reported unprompted about the same issue; that he felt that he had overdone the HPl pose. The difference between the two stances was so minuscule that the measurement was dominated by secondary movements such as supination and pronation. In other words, the FPl scan was a failure, and could not be used in the analysis.

Table 5: Axis orientation and location comparison between consecutive stances and literature reference (subject 2).

	total axis turn (|°|)	coronal AP turn (°)	axial IS turn (°)	min translation (mm)	distance on medial talar surface (mm)	distance on lateral talar surface (mm)
FDo-HDo / HDo-N	22.47	-21.54	7.21	0.26	8.5	6.7
HDo-N / N-HPl	19.83	18.12	8.77	3.40	9.9	4.5
N-HPl / HPl-FPl	~~61.54~~	-	-	~~68.14~~	-	-
lit. / FDo-HDo	3.96	4.04	-0.52	1.66	3.1	6.6
lit. / HDo-N	18.53	-17.28	6.17	2.27	11.1	2.3
lit. / N-HPl	2.53	0.51	-2.48	0.82	1.4	2.4
lit. / HPl-FPl	~~64.00~~	-	-	~~68.47~~	-	-

Table 6: Subject 2's axis lengths inside talus.

	axis length between talar surfaces (mm)
lit. reference	31.7
FDo-HDo	37.2
HDo-N	35.8
N-HPl	33.2
HPl-FPl	-

Tables 5 and 6 present the same data for subject 2 as earlier described with subject 1. Literature reference, FDo-HDo, and N-HPl axes can be seen to be grouped relatively tightly together, whereas HDo-N is twisted 22.47° and 19.83° relative to FDo-HDo and N-HPl, respectively.

7.5 Accuracy and reliability of the method

A higher quantity of patients should be studied for statistical relevance. This was not possible due to the radiation constraint limits. Ideally, the patient whose ankle was measured earlier with a coordinate measuring machine [Björkstrand et al., 2010] should have served as a golden standard. However, computed tomography imaging of his ankle proved infeasible: he was well under a progress of recuperation, and an unnecessary radiation dose of several CT scans was considered unacceptable from an ethical viewpoint. Another option was to use cadaver ankles, but access to them is limited.

In the absence of more reliable methods of result verification, an assessment of the internal reliability of the registration and matrix algebra phases was performed as described in chapter 6.2. Figures 32 and 33 present the results: it can be assessed visually that the axes are at least approximately in same positions as in figure 29 and 31. Table 7 shows the changes in the orientations and locations of the axes like table 5 did using the neutral position CT image as the static image. Furthermore, the differences between the corresponding values between the two tables are reported. The deviation between axis orientations was 0.03 degrees, and the deviation between axis locations was 0.22 mm. Such low values indicate a good potential for the method, but should not lead into too strong conclusions until more measurements are performed.

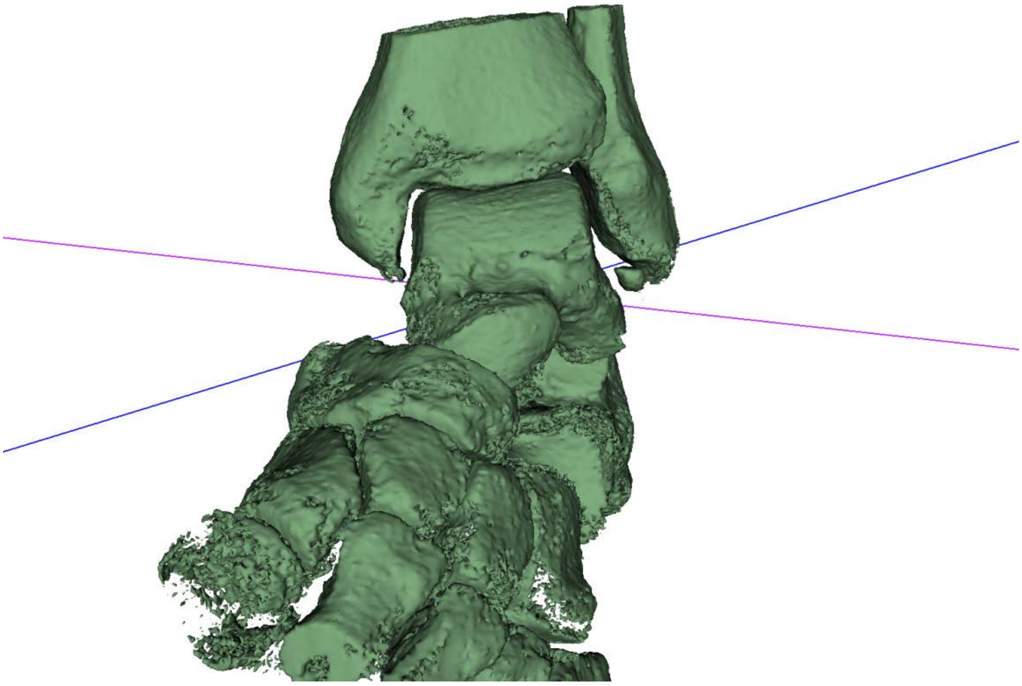

Figure 32: Finite helical axes of subject 2 recalculated with HDo stance as the global coordinate system. Purple is FDo-HDo and blue is HDo-N. Coronal (anterior) view.

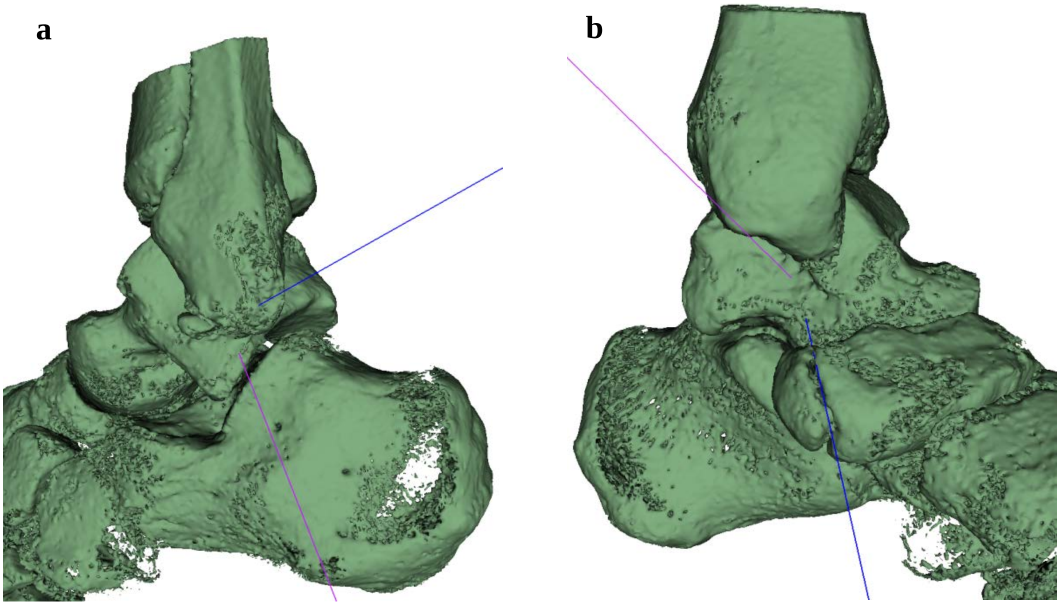

Figure 33: Finite helical axes of patient 2 recalculated with HDo stance as the global coordinate system. Purple is FDo-HDo and blue is HDo-N. (a) Lateral view and (b) medial view.

Table 7: Axis calculations in the HDo coordinate system, and comparison to earlier values.

	axis turn (°)	**Δ**	**minimum translation (mm)**	**Δ**
FDo-HDo / HDo-N (HDo coordinates)	22.50	0.03	0.04	0.22
FDo-HDo / HDo-N (neutral coordinates)	22.47		0.26	

7.6 Error analysis

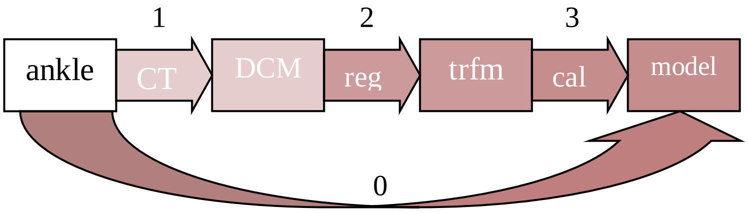

The error sources of the proposed process can be decomposed into four types. These are:

0. Joint axis simplification
As previously stated, talocrural joint is not exactly a hinge joint. Thus, approximating it as such a mechanism generates a significant error by introducing an *experimental artifact*. It can be seen as a measure for *validity* of the method – how realistically does the model approximate real human joint motion. The other types of uncertainty sources described in this chapter are collectively known as *instrumental artifacts*, describing the *reliability* of the method.

1. Inaccuracy of the CT scanning
In addition to the simplification error of the motion model, most of the total error is generated in the first step of the process, that is, the computed tomography scanning. Both spatial and contrast resolution should be maximized, but the imposed radiation dose acts as a limiting factor, as illustrated in equation 6. The most advanced medical imaging devices today reach spatial resolution around 0.2 millimeters, while industrial micro-CT scanners reach accuracies way beyond this (down to 10 µm). However, these scanners are designed for scans of smallish (<1 dm) non-living samples. The scanners in clinical use are under constant development.

Since the temporal resolution of the scans performed for this thesis was relatively low – scan time around 20 seconds per image – the images are subject to considerable motion artifact. Holding an ankle in perfectly fixed position for such a time period is not easy even for a healthy patient. One of the three analyzed images could visually be assessed to be more blurry than the others, which alludes to a minor involuntary movement during scan. In future scans, more effort needs to be made to support the ankle (as long as it is remembered that all support types create external forces, hence they may alter the patient’s natural ankle motion).

Accuracy is also affected by the operator, i.e. the clinician who performs the CT scan. Particularly, he/she should be able to detect suboptimal images (suboptimal for example due to excessive motion artifact) at spot, and in those cases take a new image. The amount of images taken cannot be increased in an uncontrolled fashion due to the radiation dose limitations; thus in practice, only clearly unsuccessful images should be retaken.

2. Imperfect image registration
This phase can be performed either automatically (algorithmically) or manually. The accuracy of automated registration depends on chosen algorithm and computation time, while the accuracy of manual registration is determined by experience and available time of the expert who performs the task. In this thesis, a rough, manual initial registration was combined with more refined automatic registration.

3. Numerical error
While registering the images, registration algorithms or software produce transform matrices of a certain precision, e.g. four decimals. These imprecise values are then imported into computation software such as MATLAB where additional error accumulates because of finite precision of the calculations, and truncation error, which is the difference between the exact mathematical solution and the approximate solution used in computation. These sources of error are collectively referred to as numerical error. This is estimated to be insignificant.

7.7 The applicability of the method for other joints

The proposed treatment process of fabrication of patient-specific fixators via additive manufacturing can be generalized for treatment of traumas of other joints, especially in lower limbs. When it comes to the complexity of its motion, the ankle joint can be considered more challenging than e.g. shoulder joint (which is a simple ball-and-socket joint) – as the results of this research and previous literature shows, the talocrural joint axis is not fixed.

The knee joint can be considered even trickier. Like the ankle joint, it does not possess a clearly defined joint center – instead, it is characterized by the femur both sliding (translation) and rolling (rotation) on the tibia. Figure 33 shows an illustration of a knee joint. The translation component is considerably larger than that in the talocrural joint. On the other hand, the range of motion is larger in the knee. This allows for bigger measurement errors, while the relative error stays the same. The CT based joint motion capture technique described in this thesis can be readily used for the knee joint as well, after substituting the tibia by the femur, and the talus by the tibia.

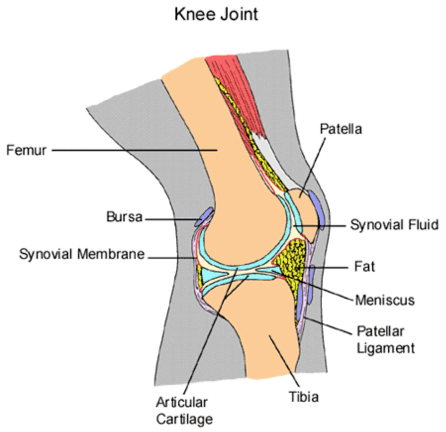

Figure 34: The knee joint.

8 Conclusions

The research group, as well as the author of this thesis, started their work with very limited knowledge of the biomechanics of the ankle. Initial assumptions included a fixed uniaxial hinge motion, and a barrel shaped talus bone. As the work progressed, the nature was found to be much more complicated, and the hypothesis of dynamically moving and rotating joint axis started to become more convincing.

The case study was successful for the most part. The results were reasonable in biological sense. However, one of the five CT scans of subject 2 (FPl) proved to be redundant, since it was too close to the HPl stance, and finite helical axis could not be computed reliably.

The measurements support to a certain degree the earlier understanding that the talocrural joint axis changes over the range of motion (from dorsiflexion to plantarflexion), and the instantaneous axes intersect inside the talus, usually closer to the lateral side than the medial side. The exact extent of translation could not be determined, but lower limits were calculated. Somewhat surprisingly, on subject 2 it was larger around the neutral stance (3.40 mm) than in dorsiflexion (0.26 mm).

However, the sample size in these analyses were too small to allow any definite conclusions – especially since it is known that intersubject variation in the ankle joint is rather high. Instead, this thesis serves as a proof of concept or a method description for computed tomography based ankle motion estimation. The research group aims to continue measurements in the future utilizing cadaver ankles, which will permit a larger sample pool since radiation dose issues are of no concern. The CT method will be compared with the coordinate measuring machine technique, with radiostereophotogrammetric (RSA) analysis serving as a gold standard.

At this point, coordinate measuring machines are assumed – although not proven yet – to offer superior accuracies compared to the CT analysis. Hence, the main question when choosing the method is: which are more essential criteria; the widespread availability in hospitals and the possibility to model the motion prior to the trauma (CT), or possibly higher accuracy (CMM)? The described computed tomography technique offers potential for further development.

References

Andersen Michael S., Benoit Daniel L., Damsgaard Michael, Ramsey Dan K., Rasmussen John (2010). *Do kinematic models reduce the effects of soft tissue artefacts in skin marker-based motion analysis? An in vivo study of knee kinematics.* Journal of Biomechanics, 43: 268-273.

Arndt A., Wolf P., Liu A., Nester C., Stacoff A., Jones R., Lundgren P., Lundberg A. (2006). *Intrinsic foot kinematics measured in vivo during the stance phase of slow running*. Journal of Biomechanics, 40: 2672-2678.

Björkstrand Roy, Tuomi Jukka, Paloheimo Markku, Lindahl Jan Erik, Salo Jari (2010). *3D-Digitalization of ankle movement and 3D-CAD-method for patient specific external ankle support development and Rapid Manufacturing*. Innovative Developments in Design and Manufacturing, 29: 199-204.

Blankevoort L., Beimers L., Jonges R., Valstar E.R., Tuijthof G.J.M. (2008). *The accuracy of a CT-based bone segmentation technique for measuring the range of motion of the joints in the ankle*. Oral presentation, Journal of Foot and Ankle Research, 1, suppl. 1: O34.

Bottlang Michael, Marsh John L., Brown T.D. (1999). *Articulated external fixation of the ankle: minimizing motion resistance by accurate axis alignment.* Journal of Biomechanics, 32: 63-70.

Bruening Dustin A., Crewe Ashlie N., Buczek Frank L. (2008). *A simple, anatomically based correction to the conventional ankle joint center*. Clinical Biomechanics, 23: 1299-1302.

Cappozzo A., Catani F., Leardini Alberto, Benedetti M.G., Della Croce U. (1996). *Position and orientation in space of bones during movement: experimental artifacts*. Clinical Biomechanics, 11: 90-100.

Chowdhry M., Porter K. (2010). *The pilon fracture*. Trauma, 12: 89-103.

Corazza Federico, Stagni Rita, Parenti Castelli Vincenzo, Leardini Alberto (2005). *Articular contact at the tibiotalar joint in passive flexion.* Journal of Biomechanics, 38: 1205-1212.

Corazza Stefano, Mündermann Lars, Gambaretto Emiliano, Ferrigno Giancarlo, Andriacchi Thomas P. (2010). *Markerless Motion Capture through Visual Hull, Articulated ICP and Subject Specific Model Generation*. International Journal of Computer Vision, 87: 156-169.

Davidson Joseph K., Hunt Kenneth H. (2004). *Robots and Screw Theory: Applications* *of Kinematics and Statics to Robotics*. Oxford University Press.

Douglas T.S., Vaughan C.L., Wynne S.M. (2004). *Three-dimensional point localization in low-dose X-ray images using stereo-photogrammetry*. Medical and Biological Engineering and Computing, 42: 37-43.

Draper C.E., Santos J.M., Kourtis L.C., Besier T.F., Fredericson M., Beaupre G.S., Gold G.E., Delp S.L. (2008). *Feasibility of Using Real-Time MRI to Measure Joint Kinematics in 1.5T and Open-Bore 0.5T Systems.* Journal of Magnetic Resonance Imaging, 28: 158-166.

European Council (1997). *Directive on medical radiation exposure limits*, EC 97/43/EURATOM.

Fitzpatrick Daniel C., Marsh J.L., Brown T.D. (1995a). *Articulated external fixation of pilon fractures: the effects on ankle joint kinematics.* Journal of Orthopaedic Trauma, 9: 76-82.

Fitzpatrick Daniel C., Foels W.S., Pedersen D.R., Marsh J.L., Saltzman C.L., Brown T.D. (1995b). *An articulated ankle external fixation system that can be aligned with the ankle axis.* Iowa Orthopaedic Journal, 15: 197-203.

Gering D., Nabavi A., Kikinis R., Grimson W., Hata N., Everett P., Jolesz F., Wells W. (1999). *An Integrated Visualization System for Surgical Planning and Guidance using Image Fusion and Interventional Imaging.* International Conference on Medical Image Computing and Computer Assisted Intervention, 2: 809-819.

Giannatsis J., Dedoussis V. (2009). *Additive fabrication technologies applied to medicine and health care: a review.* International Journal of Advanced Manufacturing Technologies, 40: 116-127.

Godfrey A., Conway R., Meagher D., O’Laighin G. (2008). *Direct measurement of human movement by accelerometry*. Medical Engineering & Physics, 30:1364-1386.

Inman Verne Thompson (2002). *The Joints of the Ankle*. 2nd edition, Williams & Wilkins.

Kozanek M., Van de Velde S.K., Gill T.J., Li G. (2008). *The contralateral knee joint in cruciate ligament deficiency.* American Journal of Sports Medicine, 36: 2151-2157.

Kruth J.-P., Leu M.C., Nakagawa T. (1998). *Progress in Additive Manufacturing and Rapid Prototyping*. Annals of the CIRP, 47/2.

Kärrholm, J. (1989). *Roentgen stereophotogrammetry – Review of orthopedic applications.* Acta Orthopaedica Scandinavica, 60: 491-503.

Leardini Alberto, O'Connor J.J., Catani F., Giannini S. (1999). *Kinematics of the human ankle complex in passive flexion; a single degree of freedom system.* Journal of Biomechanics, 32: 111-118.

Lorensen William E., Cline Harvey E. (1987). *Marching Cubes: A high resolution 3D surface construction algorithm.* Computer Graphics, 21: 4.

Lundberg Arne, Svensson Ola K., Németh Gunnar, Selvik Göran (1989). *The axis of rotation of the ankle joint.* The Journal of Bone and Joint Surgery, 71-B: 94-99.

Maintz J.B. Antoine, Viergever Max A. (1998). *A survey of Medical Image Registration.* Medical Image Analysis, 2: 1-36.

Marsh J.L., Bonar S., Nepola J.V., Decoster T.A., Hurwitz S.R. (1995). *Use of an articulated external fixator for fractures of the tibial plafond.* The Journal of Bone and Joint Surgery, 77: 1498-1509.

Mattingly Brian, Talwalkar Vishwas, Tylkowski Chester, Stevens David B., Hardy Peter A., Pienkowski David (2006). *Three-dimensional in-vivo motion of adult hind foot bones.* Journal of Biomechanics, 39: 726-733.

Mironov V., Trusk T., Kasyanov V., Little S., Swaja R., Markwald R. (2009). *Biofabrication: a 21st century manufacturing paradigm.* Biofabrication, 1.

Müller F.J., Nerlich M. (2010). *Tibial Pilon Fractures.* Acta Chirurgiae Orthopaedicae et Traumatologiae Čechoslovaca, 77: 266-276.

Mäkitie Antti, Paloheimo Kaija-Stiina, Björkstrand Roy, Salmi Mika, Kontio Risto, Salo Jari, Yan Yongnian, Paloheimo Markku, Tuomi Jukka (2010). *Teollisen pikavalmistuksen lääketieteelliset sovellukset.* Duodecim, 126: 143-151.

Nienstedt Walter, Hänninen Osmo, Artsila Antti, Björqvist Stig-Erik (1999). *Ihmisen fysiologia ja anatomia.* 12th edition, WSOY, Porvoo.

Oatis Carol A. (1988). *Biomechanics of the Foot and Ankle Under Static Conditions.* Physical Therapy, 68: 1815-1821.

O'Hara B.P., Urban J.P., Maroudas A. (1990). *Influence of cyclic loading on the nutrition of articular cartilage.* Annals of the Rheumatic Diseases, 49: 536–539.

Peolsson Michael, Löfstedt Tommy, Vogt Susanna, Stenlund Hans, Arndt Anton, Trygg Johan (2010). *Modelling human musculoskeletal functional movements using ultrasound imaging.* BMC Medical Imaging 2010, 10.

Peters Alana, Galna Brook, Sangeux Morgan, Morris Meg, Baker Richard (2010). *Quantification of soft tissue artifact in lower limb human motion analysis: A systematic review.* Gait & Posture, 31: 1-8.

Petzold R., Zeilhofer H.-F., Kalender W.A. (1999). *Rapid prototyping technology in medicine – basics and applications.* Computerized Medical Imaging and Graphics, 23: 277-284.

Pieper S., Lorensen B., Schroeder W., Kikinis R. (2006). *The NA-MIC Kit: ITK, VTK, Pipelines, Grids and 3D Slicer as an Open Platform for the Medical Image Computing Community*. Proceedings of the 3rd IEEE International Symposium on Biomedical Imaging: From Nano to Macro, 1: 698-701.

Pieper S., Halle M., Kikinis R. (2004). *3D SLICER*. Proceedings of the 1st IEEE International Symposium on Biomedical Imaging: From Nano to Macro; 1: 632-635.

Rüedi T.P., Allgöwer M. (1969). *Fracture of the lower end of the tibia into the ankle-joint*, Injury, 1: 92-99.

Salter Robert B., Simmonds D.F., Malcolm B.W., Rumble E.J., MacMichael D., Clements N.D. (1980). *The Biological Effect of Continuous Passive Motion on the Healing of Full-Thickness Defects in Articular Cartilage.* The Journal of Bone and Joint Surgery, 62: 1232-1251.

Sheehan Frances T. (2010). *The instantaneous helical axis of the subtalar and talocrural joints: a non-invasive in vivo dynamic study*. Journal of Foot and Ankle Research, 3: 13.

Siegler S., Udupa J.K., Ringleb S.I., Imhauser C.W., Hirsch B.E., Odhner D., Saha P.K., Okereke E., Roach N. (2005). *Mechanics of the ankle and subtalar joints revealed through a 3D quasi-static stress MRI technique*. Journal of Biomechanics, 38: 567-578.

Southern California Orthopedic Institute (2004). *Vermont Othopaedic Clinic, Anatomy of the Ankle* (website). Accessible at: http://www.vermontorthoclinic.org/foot.html, referred 17.8.2011.

Stefanyshyn D.J., Engsberg Jack R. (1994). *Right to left differences in the ankle joint complex range of motion*. Medicine & Science in Sports & Exercise, 26: 551-555.

Studholme Colin, Hill Derek L.G., Hawkes David J. (1999). *An Overlap Invariant Entropy Measure of 3D Medical Image Alignment,* Pattern Recognition, 32: 71-86.

TEKES (1997). *Rapid prototyping – Mallien, prototyyppien ja työkalujen pikavalmistus*. TEKES Teknologiakatsaus 52/97, Helsinki.

Tuijthof G.J., Zengerink M., Beimers L., Jonges R., Maas M., van Dijk C.N., Blankevoort L. (2009). *Determination of consistent patterns of range of motion in the ankle joint with a computed tomography stress-test.* Clinical Biomechanics, 24: 517-523.

Tuomi Jukka, Paloheimo Kaija-Stiina, Björkstrand Roy, Salmi Mika, Paloheimo Markku, Mäkitie Antti Aarni (2009). *Medical applications of Rapid Prototyping – from Applications to Classification*. Innovative Developments in Design and Manufacturing : Advanced Research in Virtual and Rapid Prototyping - Proceedings of VR@P4, Oct. 2009, Leiria, Portugal, 701-704.

Uecker M., Zhang S., Voit D., Karaus A., Merboldt K.-D., Frahm J. (2010). *Real-time MRI at a resolution of 20 ms*. NMR in Biomedicine, 23: 986-994.

Van Sint Jan S., Salvia P., Hilal I., Sholukha V., Rooze M., Clapworthy G. (2002). *Registration of 6-DOFs electrogoniometry and CT medical imaging for 3D joint modeling*, Journal of Biomechanics, 35: 1475-1484.

Webb Steve (1988). *The Physics of Medical Imaging*. Taylor & Francis.

Wohlers Terry (2010). *Wohlers Report 2010: Additive Manufacturing State of the Industry*. Wohlers Associates, Fort Collins.

Wong Yueshuen, Kim Wangdo, Ying Ning (2005). *Passive motion characteristics of the talocrural and the subtalar joint by dual Euler angles.* Journal of Biomechanics, 38: 2480-2485.

You Byoung-Moon, Siy Pepe, Anderst William, Tashman Scott (2001). *In Vivo Measurement of 3-D Skeletal Kinematics from Sequences of Biplane Radiographs: Application to Knee Kinematics*. IEEE Transactions on Medical Imaging, 20: 514-525.

Appendix A: IRTK input parameters

The Image Registration Toolkit contains an assortment of built-in registration algorithms. For bone registration, a rigid algorithm (rreg) was used, by console command like below:

```
rreg moving.nii.gz fixed.nii.gz –dofout rreg-auto.dof –dofin rreg-
manual-init.dof –Tz1 15 –Tz2 195
```

where input transform (-dofin parameter) is the initial, approximate manual registration performed in 3D Slicer. Tz-parameters limit the slices to be registered: here the registration is set to process only 181 slices of the target image (corresponding to the tibia).

Appendix B: Transformation matrices of subject 2

The ankle of subject 2 was imaged in five positions, thus yielding in total 8 registrations.

Full dorsiflexion (FDo) to half dorsiflexion (HDo)

Tibia

0.9942	-0.1030	0.0308	-17.7200
0.1053	0.9909	-0.0836	16.0000
-0.0220	0.0863	0.9960	14.0308
0	0	0	1

Talus

0.9636	0.0097	-0.2672	10.4000
0.0114	0.9969	0.0774	-1.7000
0.2671	-0.0776	0.9605	24.1000
0	0	0	1

Half dorsiflexion (HDo) to neutral (N)

Tibia

0.9999	0.0090	0.0131	-10.2000
-0.0088	0.9999	-0.0148	2.6600
-0.0132	0.0147	0.9998	-13.9900
0	0	0	1

Talus

0.9140	0.0199	-0.4052	15.2863
0.0319	0.9922	0.1206	-2.8600
0.4044	-0.1231	0.9063	15.8900
0	0	0	1

Neutral (N) to half plantarflexion (HPl)

Tibia

0.9924	0.1228	-0.0033	11.8824
-0.1227	0.9922	0.0201	-20.7000
0.0058	-0.0196	0.9998	-4.7280
0	0	0	1

Talus

0.9230	0.0279	0.3838	-28.689
0.0373	0.9862	-0.1613	7.0441
-0.3830	0.1632	0.9092	-22.360
0	0	0	1

Half plantarflexion (HPl) to full plantarflexion (FPl)

Tibia

0.9360	-0.3516	0.0193	-37.1000
0.3520	0.9328	-0.0776	23.0000
0.0093	0.0794	0.9968	3.0600
0	0	0	1

Talus

0.9248	-0.3795	0.0273	-40.330
0.3805	0.9216	-0.1542	24.6507
0.0041	0.0817	0.9966	2.8200
0	0	0	1